NSF GRANT #DMI- 01-15486
NSF PRORAM NAME: Materials Processing & Manufacturing

Flow Dynamics and Inclusion Transport in Continuous Casting of Steel

B.G. Thomas,
W. Grafton & Lillian B. Wilkins Professor
University of Illinois at Urbana-Champaign
Department of Mechanical and Industrial Engineering
1206 West Green Street, Urbana, IL 61801
Ph: 217-333-6919, 217-244-4656; Fax: 217-244-6534;
Email: bgthomas@uiuc.edu

L. Zhang (Ph.D), Q. Yuan (Ph.D), S.P. Vanka (Professor)
University of Illinois at Urbana-Champaign
Department of Mechanical and Industrial Engineering
1206 West Green Street, Urbana, IL 61801

Abstract: The formation, growth, transport, removal, and entrapment of inclusion particles have a great effect on the quality of continuous cast steel. These phenomena depend greatly on the flow dynamics. As part of a long-term effort to develop and apply comprehensive models of these and other phenomena, this paper reports on work during the third year of this NSF grant that aims 1) to develop quantitative models of transient flow of molten steel, superheat and inclusion behavior during the continuous casting of steel, and 2) to apply them to improve understanding and efficiency of inclusion particle removal in the process. Results are reported here for four interrelated subprojects, which build on work previously reported. Firstly, models of transient flow using Large Eddy Simulation (LES), which were previously validated with experiments, are validated using rigorous mesh refinement analysis. Next, the models, which were used to predict flow, transport, and removal of small inclusion particles are applied to larger particles, using a new criterion model for particle capture by a dendritic interface. Of most significance, while more large particles are removed than small ones, the capture rate as defects is still very high. Attention was then focused on other removal means. A model of inclusion capture to bubbles was developed, validated, and then applied to predict inclusion removal in the mold. Finally, the effect of mold parameters on the flow pattern is investigated, to aid in optimizing flow to avoid other defects, such as level fluctuations and re-entrainment of inclusions from the top surface.

1. Introduction: There are great economic, environmental and safety incentives for understanding how to lower the inclusion content of steel. Lowering inclusion-related defects improves steel minimum strength, fatigue life, surface appearance, yield and energy efficiency (from reduced rejects), and thereby increases competitiveness of the steel industry. Consistent lower inclusions levels would allow thinner gage products (with associated weight and energy savings) and could reduce the need for costly and energy-intensive secondary refining steps, such as vacuum arc refining and electroslag remelting. Continuous casting produces 96% of the steel manufactured in the U.S. [1] and is the last, and most important, processing step where inclusions can either be generated or removed. This project investigates

inclusion removal during this process through the use of computational models, validated with plant experiments.

Plant observations have found that many serious quality problems, including inclusion entrapment, are directly associated with the flow pattern in the mold.[2] Defects caused by nonoptimal fluid flow are even more important to the nearer-net-shape thin-slab casting processes, which are starting to transform the industry.[3] This is because higher velocities are required through a smaller inlet nozzle to cast a thin section slab with the same throughput. Thus, design and control of the fluid flow pattern in the continuous casting mold to minimize inclusions is of crucial importance to the steel industry.

The flow pattern in the mold can be controlled by many variables, including the nozzle and mold geometry, submergence depth, steel flow rate, argon injection rate, electromagnetic stirring, and flux layer properties. Many of these parameters are easy and inexpensive to change and yet have a profound influence on flow and corresponding quality. Currently, flow pattern design is done through trial and error, based on qualitative experiments with water models, plant trials, and the plant operator's experience with defects. Identifying an optimal flow pattern is very difficult, because the fundamental relationship between flow pattern and inclusion entrapment has not been quantified. Thus, each casting operation requires its own expensive experiments, and old defects often reappear when changes in the process occur. With so many different operations and new processes to optimize, the industry can no longer afford this approach.

In previous studies, the principal investigators have applied computational models to increase understanding of flow in the continuous casting mold, using both steady-state[4-21] and transient simulations.[22-29] The reliability of these models to predict flow has been demonstrated through comparison with both water models[9-11, 16, 19, 20, 24, 27, 28] and flow measurements in an operating steel caster.[26, 28] The next step is to apply these models to investigate fundamentally, the associated transport and entrapment of inclusion particles and to determine quantitative relationships between flow pattern control parameters (e.g. nozzle geometry) and particle entrapment. The current research is concerned with developing and applying such computations, combined with physical water modeling studies to validate the models and to provide further insight. Finally, plant trials are conducted to further validate the models, and to test proposed improvements. The results of this study should benefit to the steel industry by leading to increased fundamental understanding of inclusion entrapment, and to improvements in design and operating conditions that improve flow pattern in the continuous casting strand and reduce costly defects.

2. The Process: A schematic of steel processing is depicted in **Fig. 1**.[30], with a close-up of the continuous casting mold given in **Fig. 2**.

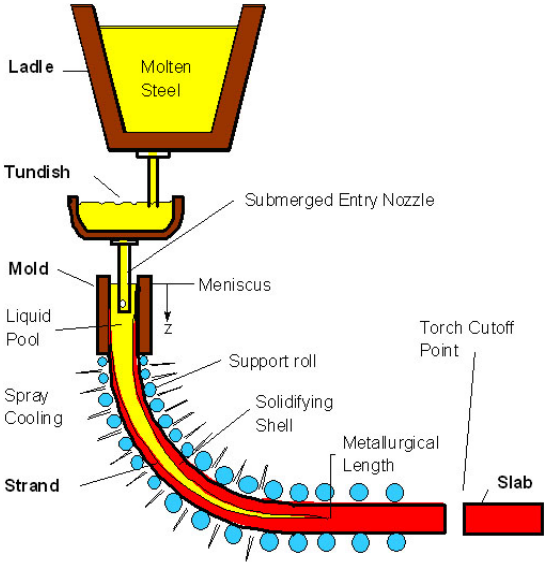

Fig. 1. Schematic of Steel Processing including ladle, tundish, and continuous casting

Steel is first refined in a ladle to remove as many dissolved impurities and particles as possible. Steel then flows from the ladle through the "tundish," and then exits down through a ceramic Submerged Entry Nozzle (SEN) and into the mold. Here, the steel freezes against the water-cooled copper walls to form a thin solid shell, which is continuously withdrawn from the bottom of the mold at a "casting speed" that matches the flow of the incoming metal. Flow through the SEN is gravity driven by the pressure difference between the liquid levels of the tundish and the mold top free surfaces. The flow rate is controlled (using feedback from a level sensor) to maintain the liquid level in the mold as constant as possible. In one method, a "stopper rod" extends down through the tundish to partially plug the exit. In another method, a "slide gate" blocks off a portion of the SEN pipe section by moving a disk-shaped plate through a horizontal slit across the entire SEN. Such flow adjustment methods allow for independent control of casting speed and metal level, and are essential for stopping the flow of molten steel if the operation must be abruptly terminated. The submerged nozzle protects the molten steel from exposure to air, which helps to avoid reoxidation and inclusion formation. Together with the casting speed, mold geometry, argon gas injection rate, and other parameters, the nozzle geometry also controls the flow

pattern created in the mold cavity. This flow pattern in turn controls the entrapment of inclusions and other defects which determine the steel quality.

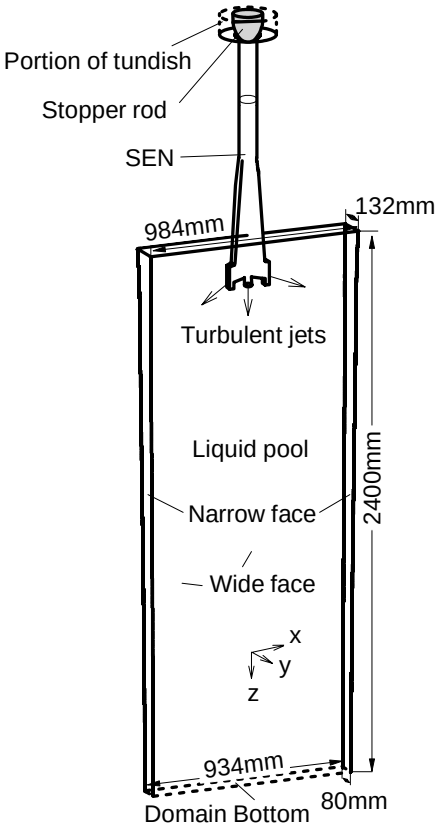

Fig. 2. Schematics of the computational domain of the thin-slab steel caster.

3. The Problem: Jets of molten steel exit the nozzle and traverse across the mold cavity to impinge on the solidifying steel shell near the narrow faces. These jets carry bubbles and inclusion particles into the mold cavity. In addition, high speed flow across the top surface may shear droplets of liquid mold slag into the flow, where they may become entrained in the liquid steel.[31] If the flow pattern enables the particles to reach the top surface, they should be harmlessly removed into the liquid slag layer. However, when the flow pattern is detrimental, particles become entrapped in the solidifying steel shell, where they cause serious quality problems and costly rejects. Particle trajectories and removal depend on particle size, which is further complicated by collisions and attachment to bubbles. Particles that become trapped near the meniscus generate surface delamination defects, and may initiate surface cracks. This problem is more likely when there are rapid fluctuations in the level of the top surface. It is also more likely when the meniscus partially freezes to form meniscus "hooks", which entrap particles into the solidifying meniscus before they can enter the liquid slag. Meniscus hooks are more prevalent there is insufficient liquid temperature at the meniscus. The local superheat of the molten steel near the meniscus depends on the flow pattern in the mold, as the jets also transport superheat.

High velocities across the meniscus are detrimental because they cause excessive surface level fluctuations, which enhances particle entrapment. High surface velocities also may entrain some of the molten slag into the steel, where it breaks up into slag inclusions. This is also controlled by the flow pattern in the mold.

Particles which are entrained into the lower recirculation zones can gradually spiral and become trapped in the solidifying front deep inside the product,[15, 32] leading to internal cracks, slivers in the final rolled product, and blisters.[2] One of these defects, known as "pencil pipes"[31] is caused when small argon gas bubbles surrounded by inclusions are caught in the solidifying shell. During rolling, the inclusion clusters elongate to create long slivers in the final product. During subsequent annealing processes, the trapped bubbles expand to create surface blisters.[31] These intermittent defects are particularly costly because they are often not detected until after many subsequent finishing steps.

There is clearly a great incentive to understand how to control the mold flow pattern in order to minimize particle entrapment and the associated quality problems. Furthermore, there are several different phenomena that may contribute to the defects, whose relative importance and mechanisms need to be quantified.

4. Previous Results: In the first two years of this project, significant advances were made on several aspects of this multifaceted research project involving dynamic flow and inclusion transport in the continuous casting mold. They are briefly summarized in the last two year's reports.[33, 34] These subprojects included in 2002: A) asymmetric transient flow in the mold, B) surface level, particle transport, and heat transfer in the molten pool; C) nucleation and growth of alumina inclusions in molten steel; D) effect of bubbles on inclusion removal; and E) inclusion removal in the steel caster and in 2003: A) Particle transport and entrapment in a continuous-cast thin slab; B) Parametric study: effect of nozzle geometry on inclusion entrapment; C) Nucleation and growth models for alumina inclusions in molten steel; D) Flow and heat transfer in a molten flux layer; and E) Transient flow and superheat transport in continuous-cast steel slabs.

5. Current Results: The results of this project are contained in 32 publications to date[33-64] and in our website http://ccc.me.uiuc.edu. This paper reports

selected recent results on four different components of the current multifaceted research project:

1) Computational Issues in Simulation of Transient Flow in Continuous Casting
2) Inclusion Transport and Entrapment in the Steel Continuous Casting Mold
3) Inclusion Removal via Bubbles in the Continuous Casting Mold
4) Parametric Study: Flow Optimization using Water Models

6. Computational Issues in Simulation of Transient Flow in Continuous Casting: Unsteady three-dimensional turbulent flow and heat transport in the liquid pool during continuous casting of steel slabs has been computed using several different computational models, domains, grids, and inlet conditions. The most advanced computations employ a large-eddy simulation code, UIFLOW with a second-order central-differencing scheme, 1.6 million nodes and a realistic simulation domain including the complete submerged entry nozzle. The model has been validated in previous work through comparison with PIV measurements in caster water models, and with velocity and temperature measurements in an operating steel caster. The model equations, boundary conditions, and numerical discretization details are given elsewhere.[55, 56]

The present computations are compared with flow measurements in a full-scale water model and with heat flux measurements in a jet impingement test problem. Results are compared between model domains of the full caster with symmetric half-caster and two-fold symmetric quarter-caster simulations. The effects of thermal buoyancy and the solidifying steel shell walls are studied independently. The effect of different inlet conditions is investigated by comparing results including nozzle simulations that are both coupled and uncoupled with the mold domain and simplified nozzle geometry. The importance of the Sub-grid scale (SGS) model for treating the small turbulent eddies is investigated through simulations with and without the Horiuti SGS K model. A rigorous grid refinement study is undertaken, which indicates criteria for choosing the element size near the walls. Accurate heat transfer predictions are more difficult to attain than accurate velocities. Finally, comparisons are made with Reynolds-averaged approaches, including standard K-ε and low Re-number K-ε model computations of the same system. The relative advantages and disadvantages of the different flow simulation methods are evaluated.

To investigate the effect of mesh refinement, LES computations were performed on six different grids, (similar to that in Fig. 2) and containing 0.02, 0.08, 0.10, 0.20, 0.40, and 0.80 million cells. Assuming symmetry between the right and left sides, the computational domain was one half of the physical domain. All simulations were performed with the SGS K-model and ignored buoyancy effects. The inlet conditions for these simulations were taken from a 100s half-nozzle simulation corresponding with the finest grid, stored every 0.001s.

The grids were all stretched with a factor of 1.01-1.03 to produce finer cells near the boundaries where they are most needed for accuracy, owing to the high local changes in gradient. This produced cell-center spacings from the wall at the critical region of jet impingement of 6mm, 3mm, 2.5mm, 2.5mm, 1.5mm and 1.5mm, for the 6 different grids respectively.

Flow patterns in the center plane of three different grids are compared in **Fig. 3**. The jet traverses across the domain to impinge on the narrow face, where it turns upward to the top surface and back towards the SEN in a classic double roll flow pattern. The two finest grids are almost identical, showing that grid independence has been achieved. The coarse grid shows an important deviation in jet direction that would have a large adverse effect on secondary calculations, such as particle motion.

To quantify the difference between grids on an equal basis, the velocities computed for each grid were first interpolated onto a 64x128 uniform-spaced grid. Errors for both the time-average and rms velocity were calculated as an average at the center plane y = 0 where the exact solution was estimated using the results from the finest grid (0.8 million cells).

The time average error results are presented in **Fig. 4a.** This error increases drastically with increasing grid spacing, which corresponds with decreasing number of cells in the grid. The error between the two finest grids averages only ~0.03m/s, although this represents a 17% difference, relative to the mean velocity in the domain, ~0.18m/s. Coarser grids have errors that are much larger than a glance at the velocity vectors would indicate.

The rms velocity error results are presented in **Fig. 4b**. This error also increases greatly with coarsening grid size. These results indicate that the mesh resolution prediction of velocity fluctuations is accurate within ~0.02m/s or ~17%. The fluctuating velocity component is almost half of the mean velocity component, indicating that turbulence is very strong. Overall, the fine mesh (0.8 million nodes) is believed to produce reasonable results for engineering purposes. A mesh of this refinement was used in subsequent simulations. Further details can be found elsewhere.[63, 64]

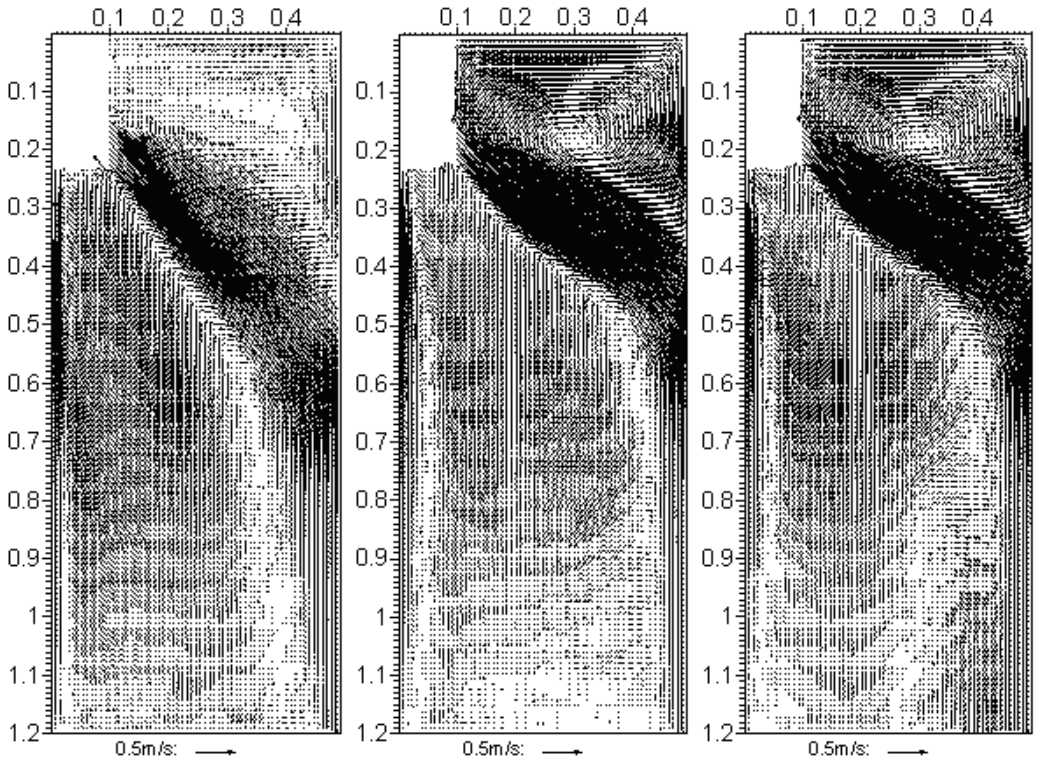

Fig.3. Time-averaged velocity fields at the center plane y=0 obtained from LES with $20x10^3$ (left) , $400x10^3$ (middle) and $800x10^3$ (right) computational cells.

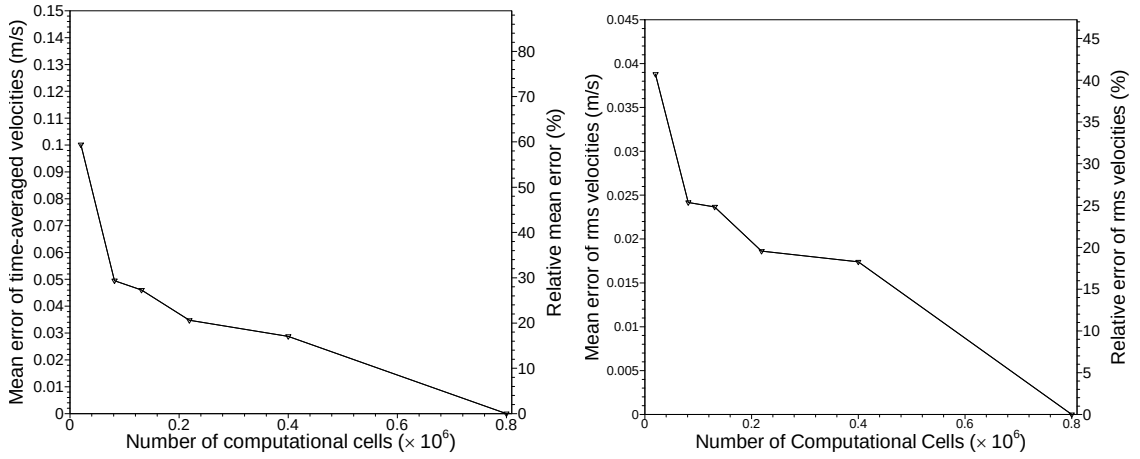

(a) (b)

Fig. 4. Effect of grid refinement on error in (a) time-averaged and (b) *rms* velocities.

7. Inclusion Transport and Entrapment in the Steel Continuous Casting Mold: The Large-Eddy_Simulation models of this project that were validated numerically (see previous section) were further extended to simulate the transient transport and entrapment of inclusion particles, based on previous computations of fluid flow in the continuous steel casting process.[52] Figure 3 shows typical time-averages of the flow patterns modeled in this study. A Lagrangian approach was developed to simulate the transport of large groups of particles through the transient flow fields. Past work on this project demonstrated validation of models of both the fluid flow and the transport of small particles using measurements in both water models and analysis of actual steel samples. The results of transport and capture of small

inclusions (10μm and 40μm) in a thin-slab steel caster are described in detail elsewhere.[53] This work showed that most of the small particles entering the mold are captured in the final product. The present work investigates the more difficult issue of the transport and entrapment of large particles, which are a greater concern for product quality.

7.1 Model Description: The geometry and operating conditions of the thin-slab caster are given in Fig. 2 and Table I. Fluid flow and particle transport were computed in the model domain (Fig. 1) that includes the 1.11m submerged entry nozzle and the top 2.40m of a steel strand (*Case 2-S*). Three dimensional time-dependent turbulent fluid velocities were first obtained by solving the Navier-Stokes equations using large eddy simulations (LES).[52] Special velocity boundary conditions [52] were applied to the fluid at the solidifying front in the steel caster to simulate the solidification effects. The transport of inclusion particles through this flow field was then modeled as follows.

7.1.1 Governing Equations: Particle transport was solved by integrating the following equations in a Lagrangian framework:

$$\mathbf{v}_p = \frac{d\mathbf{x}_p}{dt} \qquad [1]$$

$$\frac{d\mathbf{v}_p}{dt} = \frac{18\rho\nu_0}{\rho_p d_p{}^2}\left(1+0.15\,\mathrm{Re}_p{}^{0.687}\right)\left(\mathbf{v}-\mathbf{v}_p\right)+\left(1-\frac{\rho}{\rho_p}\right)\mathbf{g}+\frac{\mathbf{F}_{saff}}{m_p} \qquad [2]$$

where:

$$\mathbf{g} = (0,\ 0,\ 9.81\mathrm{m/s}^2) \qquad [3]$$

$$\mathrm{Re}_p = \frac{\left|\mathbf{v}-\mathbf{v}_p\right| d_p}{\nu_0} \qquad [4]$$

$$\mathbf{F}_{saff} = 1.61 d_p^2 \left(\mu_0\rho\right)^{1/2} \left|\boldsymbol{\omega}\right|^{-1/2}\left[\left(\mathbf{v}-\mathbf{v}_p\right)\times\boldsymbol{\omega}\right] \qquad [5]$$

and

$$\boldsymbol{\omega} = \nabla\times\mathbf{v} \qquad [6]$$

The three terms on the RHS of Eq. [2] are due to the forces of drag (for Re_p<800), buoyancy (due to density difference) and Saffman lift (due to shear velocity gradients) for spherical particles. Re_p is the Reynolds number for creeping flow, based on the small difference between the fluid and particle velocities.

7.1.2 Initial and Boundary Conditions: Inclusions were introduced into the computational domain at the local fluid velocity. Their initial positions were chosen randomly in the edges of a cylindrical region in the tundish above the submerged entry nozzle. The results of the separate simulation of fluid flow and particle trajectories in the nozzle itself were used to determine the particle locations in the nozzle outlet port planes for the strand simulation. Inclusions touching the top surface were assumed to be removed.

7.1.3 Modeling of Particle Capture by the Solidification Front: Particles that reach the mushy zone front may be trapped by the solidifying shell or repulsed back into the molten steel flow. The outcome between capture and pushing depends on many phenomena, including the morphology of the solidifying dendrites, the interfacial surface tension governed by the concentration boundary layer of the interfacial active solute (especially the sulfur content), the boundary layer velocity profile, and the particle velocity, size, density and morphology. The flow velocities close to the dendritic interface can be estimated from the LES model during the simulation. However, accurate resolution of the dendrite shape and the concentration boundary layer is computationally prohibitive. To overcome this problem, a novel, but simple criterion for particle pushing and capture has been developed in this work, based on a force balance analysis.

Particles Smaller than the PDAS: Particles smaller than the primary dendrite arm spacing (PDAS), (i.e. $2R_p$<PDAS), can easily flow in between the dendrite arms without major disturbance of their growth. Larger particles cannot do this. If the particle is smaller than the PDAS, it will be surrounded by the growing dendrites, and it will be captured whenever it reaches the solidification front. The attractive force generated by the surface energy gradient further encourages this to happen. Previous experimental studies [65] in quiescent solidification systems confirm that particles smaller than the PDAS are entrapped, even when the dendrite growth speed is much lower than the critical value for particle pushing. Therefore, a particle smaller than the PDAS is modeled as being captured by the shell whenever it touches a computational boundary representing a mushy zone (solidification) interface.

Particles Larger than the PDAS: Unlike smaller particles, particles larger than the local PDAS cannot fit between the dendrite arms. Figure 5 shows a typical dendritic front shape.[66] As depicted in Figure 5, a spherical particle of alumina or slag transported to the solidification front contacts the solidifying dendrites through a thin film of liquid steel at the critical distance. If all of the forces acting on the particle are in stable equilibrium, then it will eventually be captured by the solidifying shell as the dendrites grow to surround it. The particle will avoid being captured if the net force acting in the solidification direction push it away from the interface, or if the net force acting across the dendrite front causes it to rotate away. These conditions are

checked by considering the balance of the ten different forces which act on the particle in the boundary layer region, including the bulk hydrodynamic forces (lift F_L, pressure gradient, stress gradient, Basset, and added mass forces), transverse drag force F_D, (caused by fluid flow across the dendrite interface), gravity (buoyancy) force F_B, and the forces acting at the interface (Van der Waals interfacial force F_I, lubrication drag force F_{Lub}, and surface energy gradient force F_{Grad}).

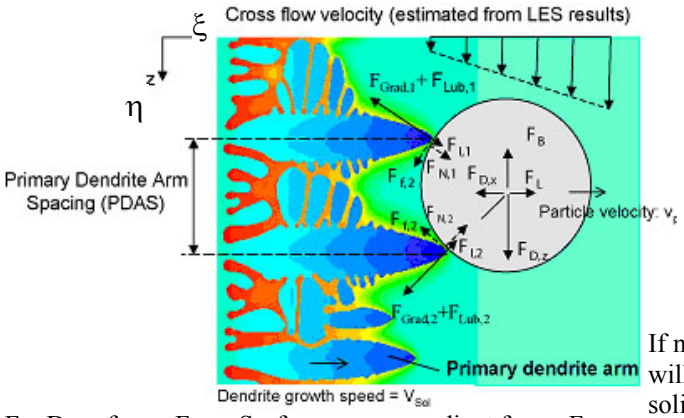

F_D: Drag force; F_{Grad}: Surface energy gradient force; F_I: Van der Waals interfacial force; F_{Lub}: Lubrication drag force; F_L: Lift force; F_B: Buoyancy force; F_N: Reaction force; F_f: Friction force.

Fig.5. Illustration of forces acting on a particle in front of solidifying dendrites.

The pressure gradient, stress gradient, Basset, and added mass forces are negligible because they are found to be small (<15% of the buoyancy force) in the bulk region, and are expected to be even smaller in the boundary layer. The condition of particle pushing or capture is determined through the following procedure:

Step 1: If the component of the total force (F_{Tot}) acting on the particle in the solidification direction (χ in Figure 5) is larger than zero, then the particle will be pushed away from the interface. This escape criterion is expressed as follows:

$$F_{Tot,\chi} = F_L - F_{D,\chi} - 2\left(F_{Lub} - F_{Grad} - F_I\right)\cos\theta > 0 \qquad [7]$$

where: $$\theta = acr\sin\left[0.5\text{PDAS} \Big/ \left(R_p + r_d\right)\right] \qquad [8]$$

Otherwise, check if the forces on the particle are large enough to avoid entrapment by pushing it along the interface.

Step 2: If $F_{Tot},\chi \le 0$, then the forces acting in η direction (across the solidification front) push the particle against a dendrite arm, causing a reaction force ($F_{N,1}$ or $F_{N,2}$) and a friction force ($F_{f,1}$ or $F_{f,2}$) at the contact point, as shown in Figure 5. If furthermore, the net forces rotating the particle about the contact points push it towards the dendrites, then the particle will not move and it will eventually become surrounded by the growing interface and captured. Specifically, capture occurs by this criterion if one of the following two conditions holds:

(1) If the buoyancy (F_B) and the η component of the drag ($F_{D,\eta}$) are in the same direction and:

$$\left(F_{D,\eta} + F_{B,\eta}\right)\cos\theta + \left(F_L - F_\chi\right)\sin\theta \le \left(F_{Lub} - F_{Grad} - F_I\right)\sin 2\theta \qquad [9]$$

(2) If the buoyancy (F_B) and the η component of the drag ($F_{D,\eta}$) are in opposite directions, and either:

$$\left(F_{D,\eta} - F_B\right)\cos\theta + \left(F_L - F_\chi\right)\sin\theta \le \left(F_{Lub} - F_{Grad} - F_I\right)\sin 2\theta, \text{ if } F_{D,\eta} \ge F_B \qquad [10]$$

or

$$\left(F_B - F_{D,\eta}\right)\cos\theta + \left(F_L - F_\chi\right)\sin\theta \le \left(F_{Lub} - F_{Grad} - F_I\right)\sin 2\theta, \text{ if } F_B > F_{D,\eta} \qquad [11]$$

If neither inequality in step 2 is satisfied, then the particle will escape by rotating about a dendrite tip away from the solidification front and drifting back into the flow. These equations, based on a two-dimensional balance, were found to represent an intermediate case between the variety of conditions that are possible when the full three-dimensional balance was calculated, as given elsewhere.[67]

The primary dendrite arm spacing needed for this analysis is found from measurements conducted on cast steel, and the dendrite tip radius (r_d) is fitted from corresponding relations.[68] Calculations show that the Van der Waals interfacial force, the lubrication drag force and the surface energy gradient force are only important when the particle is very close to the solidification interface. Therefore, they can be neglected in the Lagrangian particle transport simulations. These forces are important, however, for evaluating the capture criterion to predict the fate of a particle when it touches a computational boundary representing a mushy zone front.

The results presented previously considered particles smaller than the PDAS (50-140 μm) which can easily enter in between primary dendrite arms and become entrapped with little chance of being pushed away regardless of solidification front velocity.[69] This report focuses on larger particles (100, 250, and 400μm in diameter), which are much more difficult to capture, especially when there is a large transverse velocity.

7.1.4 Solution Procedure: The particle transport equations were integrated using the fourth order Runge-Kutta method.[70] Particle velocities and displacements were solved at every time step after the fluid velocity field was solved. The local fluid velocity in the drag and lift terms of Eq.[2] was interpolated from the nearest

neighbor cells using a second order scheme.[70] Due to the low volume fraction of impurity inclusions for the continuous casting process (~0.01% for a typical steel with 30ppm oxygen), one-way coupling was employed, which neglects the modification of fluid turbulence by the particles. The removal and capture criteria were tested whenever a particle crossed a domain boundary.

7.2 Capture Criterion Model Validation: The particle capture model was tested by applying it in simulations of several different experimental systems where particle capture was measured. Firstly, the model predictions of the critical velocity of the solidification front for the transition from particle pushing to particle capture were compared with measurements of alumina particles in quiescent solidifying liquid steel [71] and zirconia particles in quiescent solidifying aluminum melt.[72] Simulations were then conducted to reproduce the results of the capture or flow of PMMA particles in solidifying water with a tangential (cross) flow across the interfacial front.[73, 74] Both system produced reasonable results, as described in detail elsewhere.[67]

7.3 Predicted Critical Cross-Flow Velocities in Continuous Steel Caster: Using the validated particle-capture criterion, the critical velocities of the flow relative to the downward moving shell for the capture of slag spheres were computed for typical conditions in a steel caster. The flow was assumed to be vertical (upwards or downwards) across a horizontally-growing solidification front, such as encountered near the narrow face in the continuous casting mold region. The results are shown in Figure 6 for the effect of PDAS and a complete range of particle sizes for typical solidification conditions (200μm/s solidification speed and 3.4μm tip radius).

The results illustrate how capture always occurs for particles smaller than the PDAS. Particles larger than the PDAS will be captured if the magnitude of the relative cross-flow velocity between the particle and the solidifying steel shell is smaller than a critical velocity. The magnitude of this critical velocity of the fluid decreases with increasing particle size and decreasing PDAS. Velocity magnitudes higher than the critical value prevent capture, transporting the particle away from the interface before it can get entrapped. This critical velocity depends on the flow direction. Higher critical velocity magnitudes indicate easier capture. Particles are more easily entrapped in downward flow, resulting in higher critical velocity. This is because the upward buoyancy lowers the magnitude of the particle velocity (relative to that for upward flow conditions). The wedge-shaped region of the graph indicates where the capture of large particles is possible. This region becomes narrower as particle size increases, owing to the decreasing ability of the dendrite arms to prevent the rotation of large particles. This region also becomes narrower with decreasing PDAS, again due to easier rotation of particles. The wedge tends towards the terminal velocity of the particle. When the upward terminal velocity equals the downward flow speed (relative to the solidifying shell which is itself moving downwards at the casting speed), then the particle will be stationary relative to the dendrites, so can always be captured (based on results for quiescent flow.[67] With increasing velocity of the solidification front, particle capture becomes easier so the magnitude of the critical cross-flow velocity increases.[67] This effect is small compared with that of particle size, however. This simple, but comprehensive capture model is ready to help predict particle behavior in real castings over a wide range of conditions.

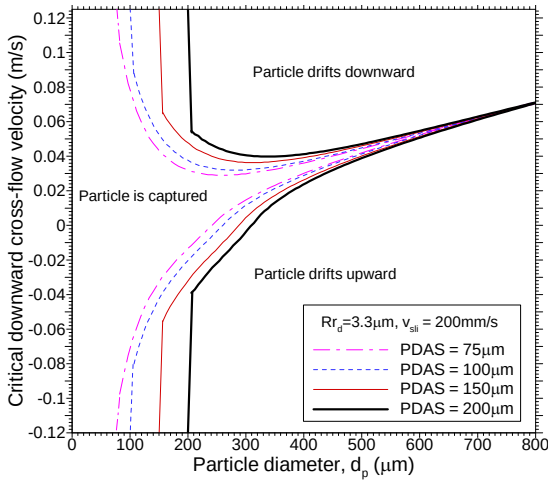

Fig.6.Critical downward cross-flow velocities for slag droplets in molten steel.

7.4 Particle Transport, Removal and Capture in the Thin-Slab Caster: The complete LES model with particle transport and capture criterion was then applied to simulate the transport and capture of three groups of 10,000 inclusions, with 2700 kg/m3 density and three different sizes (100, 250, and 400μm) in a thin slab steel caster (Fig. 1). These inclusions could represent entrained mold slag or alumina particles that entered the mold through the nozzle over a 9s interval. The computational domain has two portions. The nozzle domain includes part of the bottom of the tundish and the entire 1.11m long trifurcated submerged entry nozzle. The strand domain includes the top 2.4m of the molten pool in the mold and strand. This 2.4m computational domain is part of the 3m straight section of the real caster. The internal liquid pool domain shape was curved to account for the shell, and had mass flowing through it to represent solidification. The shell thickness increases from 0 at the meniscus to 26mm (wide face) or 25mm (narrow face) at domain exit, according to measured profiles.[52]

Elastic re-bound was assumed when a particle hit the plastic wall of the water model or the outer surface of the nozzle in steel casters. Particles touching the top surface were assumed to be safely removed by the slag layer. The particle capture criterion was tested each time a particle touched a boundary representing the solidifying shell. If the result was particle pushing, then the particle was artificially forwarded into the fluid by a distance of 5% particle radius. More information on casting conditions, material properties and computational parameters on both cases is given in Table I. Methodologies were implemented to optimize the time step size and computational cost, according to the particle response time. Both the flow simulations (1.3M cells) and the transport of 30,000 particles took about 29.2 CPUs per fluid time step (0.001s). Further details of the simulations are given elsewhere.[55, 56, 67]

7.4.1 Particle Injection through nozzle: After demonstrating the accuracy of this computational model of particle transport in a standard-slab water model, [55], and applying it to investigate the transport and capture of small inclusions in the actual thin slab steel caster[16, 53, 75], it was next applied to investigate the transport, removal and entrapment of large inclusions. The fluid velocities were obtained from LES [52] and conditions are given in Table I.

A typical snapshot of the simulated particle distribution is shown in Figure 7 a) (18s after injection of the first particle from the nozzle exit plane). This snapshot is similar to those for small particles presented elsewhere.[55] While they move with the flow, the particles gradually spread apart from the local turbulent eddies. Significant asymmetrical distribution is seen in the lower region. This asymmetry is caused by the unbalanced flow between the two halves of the lower region. The larger downward flow velocities in the right half of Figure 7 persisted for more than 50s before the flow became balanced for some time. Then, a similar unbalanced flow pattern occurred again after another 70s. This strong persistent asymmetrical flow deep in the lower recirculation region, was also observed in water models, such as by Gupta and Lahari.[76]

Figure 8 shows the removal histories for the 100-400μm particles. More large (400μm) particles were transported to the upper recirculation region and floated to the top surface than small ones (100μm). This is due to two factors. Firstly, the larger particles have larger terminal velocities: the terminal velocities for the 100μm, 250μm and 400μm slag spheres in liquid steel are estimated to be 3.9mm/s, 17.9mm/s and 33.5mm/s respectively, based on equating the drag and buoyancy forces. Secondly, the larger particles are more difficult to capture, as shown in Fig. 6.

Table I. Properties and conditions of the particle simulation in the thin-slab steel caster.

Parameter/Property	Value
Mold Width (mm)	984
Mold Thickness (mm)	132
Mold Length (mm)	1200
Domain Width (mm)	
- top	984
- bottom	934.04
Domain Thickness (mm)	
- top	132
- bottom	79.48
Domain Length (mm)	2400
Nozzle Port Height × Thickness (mm × mm)	75 × 32 (inner bore)
Bottom nozzle Port Diameter (mm)	32
SEN Submergence Depth (mm)	127
Casting Speed (mm/s)	25.4
Fluid Dynamic Viscosity (m^2/s)	7.98×10^{-7}
Fluid Density (kg/m^3)	7020
Particle Density (kg/m^3)	2700
Particle Diameter (μm)	100, 250 and 400

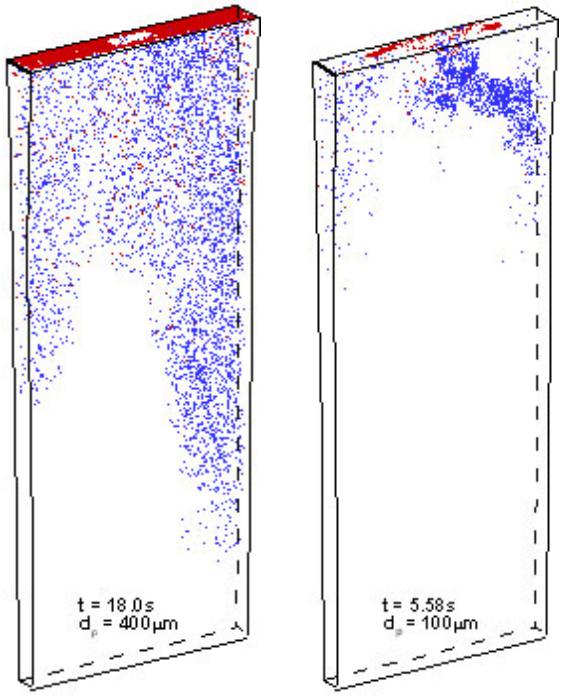

Fig.7. Snapshot of distribution of slag particles in the steel caster for a) 400 μm particles entering through the nozzle and b) 100 μm particles entrained at the top surface.

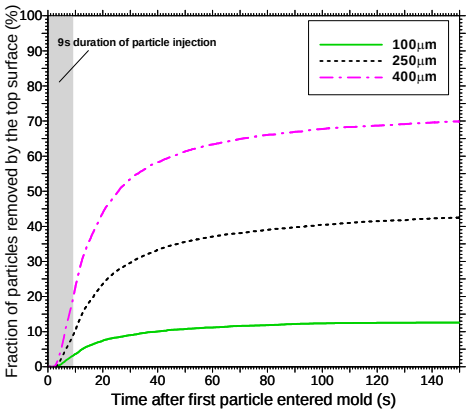

Fig.8. Removal and entrapment histories of large particles (≥100μm) which entered the mold region from nozzle ports.

Most (~90%) of the particle removal occurred in the first ~50s after the first particle entered the domain. Most (90%) of the captured particles traveled with the flow for less than ~70s. The final removal fractions were 12.6%, 42.5% and 69.9% for the 100, 250 and 400μm particles respectively. These results are consistent with plant observations that particles with sizes ranging from 50μm to 200μm are the main cause of inclusion defects in steel slabs.

The results shown here suggest that very large particles can be effectively removed from the mold region. This is known to be the case for straight-walled casters, and is the reason that many companies have invested in changing their top sections from curved to vertical. Alternatively, the less-buoyant smaller particles always experience small removal fractions. These cause less quality problems owing to their smaller size. Intermediate-sized particles of 100μm - 250μm are large enough to cause severe quality problems, yet are predicted to have high entrapment fractions, even in a vertical caster. Thus, it is important that they are removed from the steel prior to entering the mold. This conclusion may differ if gas bubbles are present, so the effects of gas injection are investigated in a later section.

7.4.2 Slag entrainment from top surface: During the actual continuous casting process, fingers of the liquid slag layer may be emulsified into the liquid steel from the top surface mold slag layer and broken into spheres by the flow. This is an important alternative source of mold slag inclusions, in addition to those entering the nozzle from upstream. To model this, a computation was conducted where three groups of 4,000 particles with sizes of 100μm, 250μm and 400 μm entered the domain near the center of the top surface, where such emulsification most likely occurs. The particles were injected computationally over 1.8s into two symmetrical 20mm×6mm×7mm(x×y×z) volumes located just below the top surface. The height of the two volumes was chosen based on the measured steel-slag interface profile.[55]

Figure 7 b) presents a typical snapshot of the distribution of the 100μm particles, 5.6s after entrainment. Again, blue dots denote moving particles and red represents the removed or captured ones. It is seen that immediately after the injection, some of the particles floated to the top surface and were consequently removed. The other particles followed the flow in the upper recirculation region, joined the oblique jet, and then behaved as if they were injected from the nozzle ports. More than 95% of the 400μm particles were safely removed in the first 2s after being entrained into the flow from the top surface slag layer. The final removal fractions exceeded 92% for particles 250μm or larger. However, the removal fraction dropped to 44.6% for the less buoyant 100μm particles. This finding demonstrates that it is very important to control fluid flow in the mold in order to avoid the entrainment of additional mold slag inclusions.

7.5 Conclusions: Lagrangian computations of particle transport during continuous casting of steel slabs were performed in this study, based on time-dependent fluid velocity fields obtained from LES. For the casting conditions simulated here, the results reveal that:

- Particle entrapment by a solidification front depends on many factors including the particle size and density, transverse fluid velocity, sulfur concentration gradient, solidification front velocity, and primary dendrite arm spacing. A new capture criterion based on a balance of the important forces acting on a particle near a solidification front has been developed, validated with test problems and applied to simulate particle capture in a steel continuous caster.
- Increasing the number of particles improves the accuracy of removal predictions, especially for later times (e.g. 10-100s). At least 2500 particles are required to obtain accuracy within ±3%. Particle removal at short times (e.g. ≤10s) is governed by chaotic fluctuations of the flow, which generate variations of ±5%.
- After a 9s sudden burst of particles enters the steel caster, about 4 minutes are needed for all of them to be captured or removed. The captured particles concentrate mainly within a 2-m long section of slab.

- Most of the inclusions trapped in the steel slab are concentrated within 10-20mm beneath the slab surface, especially at the corner, and towards the narrow faces.
- The safe removal of inclusion particles to the top surface decreases greatly with decreasing particle size. Although the removal fraction of 400 μm particles is 70%, only ~12% of 100 μm particles are removed. Only 8% of small particles (10μm and 40μm) are removed.
- The removal of slag particles entrained from the top surface depends greatly on the particle size. Most (>92%) of the 250μm - 400μm droplets simply return to the slag layer. However, more than half of the 100μm particles are eventually captured, leading to sliver defects.

8. Inclusion Removal by Bubble Flotation in Continuous Casting Mold: Fundamentally-based computational models are developed to quantify the removal of inclusions by bubbles during the continuous casting of steel. First, the attachment probability of inclusions on a bubble surface is investigated based on fundamental fluid flow simulations, incorporating the turbulent inclusion trajectory and sliding time of each individual inclusion along the bubble surface as a function of particle and bubble size. Then, the turbulent fluid flow in a typical continuous casting mold, trajectories of bubbles and their path length in the mold are calculated. The change in inclusion distribution due to removal by bubble transport in the mold is then calculated based on the computed attachment probability of inclusion on each bubble and the computed path length of the bubbles. In addition to quantifying inclusion removal for many different cases, the results are important to estimate the significance of different inclusion removal mechanisms.

8.1 Inclusion-Bubble Interactions in Molten Steel: In molten steel, bubbles smaller than 3mm tend to be spherical, 3-10mm bubbles are spheroidal, and bubbles larger than 10mm are spherical–cap shaped. The bubble size depends mainly on the gas flow rate, injection method and stirring power in the molten steel. The average equivalent size of bubbles is estimated to be ~5mm in the CC mold investigated in this work.

The attachment process of an inclusion to a gas bubble in the molten steel proceeds through the following steps: the inclusion approaches the gas bubble, and collides if it gets close enough. If the thin film of liquid between the particle and the bubble decreases to less than a critical thickness, it will suddenly rupture causing the inclusion to attach permanently to the surface of the bubble during the collision. Alternatively, if it slides along the surface of the bubble for a long enough time, the thin film can drain away and rupture, again leading to inclusion attachment. Otherwise, the inclusion will move away and detach from the bubble.

In order to calculate the interaction time and the attachment probability of inclusions to the bubble surface, a computational simulation of turbulent flow around an individual bubble is required, in addition to a simulation of the transport of a representative group of inclusions through the flow field. First, the steady turbulent fluid flow of molten steel around an argon bubble is calculated. The inlet velocity and far-field velocity condition are set to of the bubble terminal velocity, assuming a suitable turbulent energy and dissipation rate, and a far field pressure outlet. The trajectory of each particle is then calculated by Eq.[2]). To incorporate the "stochastic" effect of turbulent fluctuations on the particle motion, this work uses the "random walk" model in FLUENT.[77] In this model, particle velocity fluctuations are based on a random number chosen according to the local turbulent kinetic energy. The random number is changed, thus producing a new instantaneous velocity fluctuation, at a frequency equal to the characteristic lifetime of the eddy. The instantaneous fluid velocity is given by

$$u = \bar{u} + \xi\sqrt{2k/3}\,, \qquad [12]$$

where u is the instantaneous fluid velocity, m/s; $\bar{u}$ is the mean fluid phase velocity, m/s; ξ is a random number with a Gaussian distribution and standard deviation of 1, and k is the local level of turbulent kinetic energy in m^2/s^2.

As boundary conditions, inclusions reflect if they touch the surface of the bubble. Several thousand inclusions are uniformly injected into the domain in the column with diameter d_B+2d_p for non-stochastic model and far larger column than d_B+2d_p for stochastic model. The inclusions are injected with the local velocity at an axial distance of 15-20 times the bubble diameter from the bubble center. Attachment is assumed to occur when the interaction time between the inclusions and the bubble is larger than the film rupture time.

The attachment probability, shown in Figure 9, is defined as the fraction of particles in the column traversed by the path of the bubble that are captured onto the bubble surface. It can be obtained by

$$P = \frac{\sum_i P_i A_i}{A_{B+2P}} = \frac{\sum_i \left[\frac{N_{o,i}}{N_{T,i}} \left(\pi (R_i + \Delta R)^2 - \pi R_i^2 \right) \right]}{\frac{\pi (d_B + 2d_p)^2}{4}}, \quad [13]$$

$$= \frac{\sum_i \left[4 \frac{N_{o,i}}{N_{T,i}} \left(2R_i \cdot \Delta R_i + \Delta R_i^2 \right) \right]}{(d_B + 2d_p)^2}$$

where N_{oi} is the number of inclusions attaching to the bubble,); A_{B+2P} is the section area of the column with diameter of d_B+2d_P. N_{Ti} is the total number of inclusions injected through area A_i, and i is the sequence number of the annular position at which the inclusions are injected.

The results given here are based on the following parameters: ρ=7020 kg/m^3, ρ_P=2800 kg/m^3, ρ_g=1.6228kg/m^3, σ=1.40 N/m, θ=112^o, μ=0.0067 kg/m-s, d_p=1-100μm, and d_B=1-10mm. These parameters represent typical spherical solid inclusions such as silica or alumina in molten steel. Note that the calculation includes the phenomena that some particles in the column-shaped path of the bubble escape capture, while others outside of the column are.

The attachment probability of different-sized inclusions (d_P=5, 10, 20, 35, 50, 70,100μm) to different-sized bubbles (1, 2, 4, 6, 10mm diameter) are calculated from the inclusion trajectories computed in two different ways. Figure 10 shows results without considering the stochastic effect. This figure indicates that smaller bubbles and larger inclusions have larger attachment probabilities. Specifically, 1mm bubbles can have inclusion attachment probability as high as 30%, while the inclusion attachment probability to >5mm bubbles is less than 1%. A minimum-efficiency bubble size exists of ~7mm. Smaller bubbles attach more inclusions, owing to their higher surface area to volume ratio. Large bubbles are more efficient because of their spherical-cap shape.

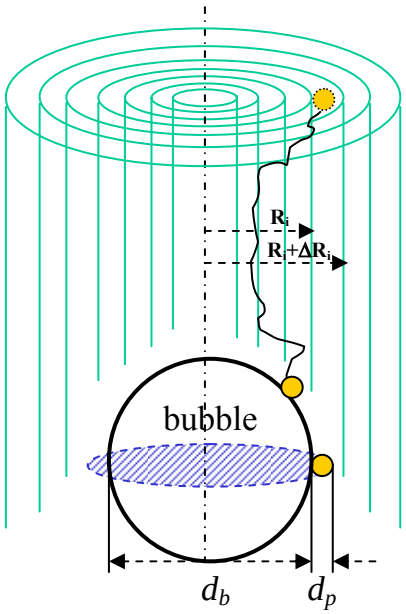

Fig.9 Schematic of the attachment probability of inclusions to the bubble surface.

To enable computation of attachment rates for a continuous size distribution of inclusions and bubbles, regression was performed on these calculated attachment probabilities. The regression equation obtained, Eq.[14], is included in Fig.10.

$$P = A d_p^B \quad [14]$$

where A and B are

$$A = 0.268 - 0.0737 d_B + 0.0615 d_B^2 \quad [15]$$

$$B = 1.077 d_B^{-0.334} \quad [16]$$

where d_B is in mm, d_p is in μm.

The simulation results indicate that the Stochastic effect increases the attachment of inclusions to the bubble surface by around 1.4 times, relative to these predictions of the non-Stochastic model.

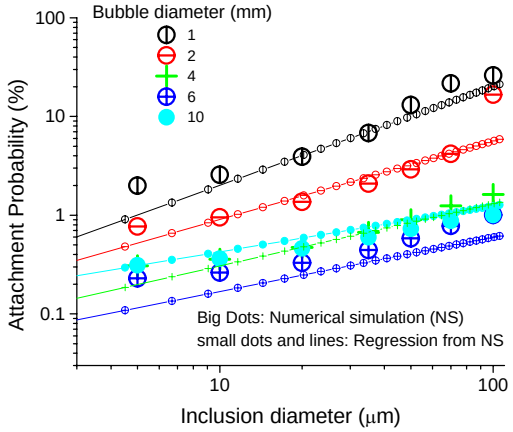

Fig.10 The calculated and regressed attachment probability of inclusions to bubbles

8.2 Fluid Flow and Bubble Motion in the Continuous Casting Strand: The three-dimensional single phase steady turbulent fluid flow in the SEN and CC strand is calculated by solving the continuity equation, Navier-Stokes equations, and equations for turbulent kinetic energy and its dissipation.[33, 34, 55] The bubble trajectories are calculated by Eq.[2], including the effect of chaotic turbulent motion using the random walk method (Eq.[12]). Bubbles escape at the top surface or the open bottom, and are reflected at other faces. The SEN has 80mm bore size, 15° downward outport angle, and 65×80mm outports. The SEN submergence depth is 300mm, and the casting speed is 1.2 m/min. Assuming symmetry, half of the mold width is simulated in the current study (2.55m length ×0.65m half width×0.25m thickness). The calculated weighted average turbulent energy and its dissipation rate at the SEN outport are 0.20 m^2/s^3 and 5.27 m^2/s^3 respectively. The calculated velocity vector distribution on the center face of the half strand indicates a double roll flow pattern. The calculated weighted average turbulent energy and its dissipation rate in the CC strand is 1.65×10^{-3} m^2/s^2 and 4.22×10^{-3} m^2/s^2 respectively. The calculation results indicate that smaller bubbles penetrate and circulate more deeply than the larger ones. Bubbles larger than 1mm mainly move in the upper roll. 0.2mm bubbles can move with paths as long as 6.65m for a time of 71.5s before they escape from the top or become entrapped through the bottom, while 0.5mm bubbles move 3.34m during 21.62s, 1mm bubbles move 1.67m during 9.2s, and 5mm bubbles move 0.59m during 0.59s. The mean of the path length (L_B) and the residence time (t_B) of the bubbles depend on the bubble size as follows:

$$L_B = 9.683\exp\left(-\frac{1000d_B}{0.418}\right)+0.595 \qquad [17]$$

$$t_B = 195.6\exp\left(-\frac{1000d_B}{0.149}\right)+ 23.65\exp\left(-\frac{1000d_B}{0.139}\right) + 2.409\exp\left(-\frac{1000d_B}{8.959}\right) \qquad [18]$$

where the path length L_B and bubble size d_B are in m, and the residence time t_B is in s.

8.3 Inclusion Removal by Bubbles in the CC Strand:

8.3.1 Model Formulation: A removal model of inclusions from the molten steel by bubble flotation is developed for the molten steel inclusions-argon bubbles system. The following assumptions are used:

- Bubbles all have the same size;
- Inclusions have a size distribution, are uniformly distributed in the molten steel, and are too small to affect bubble motion or the flow pattern;
- Only the inclusions removed by bubble flotation are considered. The transport and collision of inclusions are ignored.
- The bubble size and the gas flow rate are chosen independently;
- Once stable attachment occurs between a bubble and an inclusion, there is no detachment and the inclusion is considered to be removed from the molten steel, owing to the high removal fraction of most bubbles.

Assuming that all inclusions are Al_2O_3, the oxygen (in ppm) removed by a bubble with diameter of d_B (in m) can be expressed by

$$\Delta O = \sum_i \left[\frac{\left(\frac{\pi}{4}d_B^2\right)L_B \cdot n_{p,i} \cdot \frac{P_i}{100}}{\frac{V_C}{60}S \cdot t_B}\left(\frac{\pi}{6}d_{p,i}^3\right)\frac{\rho_p}{\rho_M}\cdot\frac{48}{102}\cdot 10^6 \right] \qquad [19]$$

where d_p is inclusion diameter in m, L_B is the path length of the bubble (m), given by Eq.[17], and P is the attachment probability of inclusion to the bubble (%), given by Eq.[14], and n_p is the number density of that inclusion size in m^{-3}, V_C is casting speed in m/min, S is the area of the slab section (=0.25×1.3m^2), t_B is the bubble residence time in second, given by Eq.[18]. ρ_M and ρ_P are densities of the molten steel and inclusions respectively.

Therefore the total oxygen removal can be expressed by

$$\Delta O = 1.16\times10^5 \cdot \frac{1}{V_C S}\frac{d_B^2 L_B}{t_B}\frac{\rho_p}{\rho_M}\sum_{j=1}^{n_B}\left[\sum_i \left(n_{p,i}\big|_j \cdot P_{A,i}\cdot d_{p,i}^3\right)\right] \qquad [20]$$

where n_B is the total number of bubbles with diameter d_B entering the molten steel during time t_B , given by

$$n_B = \frac{3}{273\pi} Q_G T_M \frac{t_B}{d_B^3} \quad [21]$$

where Q_G is the gas flow in Nl/min, T_M is the steel temperature (1823K), and the factor of ½ is due to the simulation domain of a half mold.

In Eq.[20], $n_{p,i}\Big|_j$ is the number density of inclusions with diameter $d_{p,i}$ when bubble j is injected, which can be represented by

$$n_{p,i}\Big|_j = n_{p,i}\Big|_{j-1} \times \frac{(100 - P_i)}{100} \times \frac{\left(\frac{\pi}{4} d_B^2\right) L_B}{\frac{V_C}{60} S \cdot t_B} \quad [22]$$

This equation updates the inclusion number density distribution after the calculation of each individual bubble, in order to account for the significant change in inclusion concentration caused by the simultaneous inclusion removal of many bubbles.

8.3.2 Results and Discussion: The inclusion size distributions measured in the tundish above the outlets and in the CC slab are shown in Figure 11 together with the calculated size distributions after inclusion removal by bubble flotation for several different bubble sizes. The corresponding inclusion removal fractions are shown in the adjacent frame. If the bubbles were larger than 5mm, less than 10% of the inclusions can be removed by bubble flotation at the gas flow rate of 15 Nl/min. This corresponds to a 3ppm decrease in total oxygen. Smaller bubbles appear to cause more inclusion removal for the same gas flow rate. Specifically, 1mm bubbles remove almost all of the inclusions larger than 30μm. However, it is unlikely that all of the bubbles that are this small could escape from the top surface. Those that are entrapped in the solidifying shell would generate serious defects in the steel product. Increasing bubble size above ~7mm produces no change in removal rate, likely due to the change in bubble shape offsetting the smaller number of bubbles.

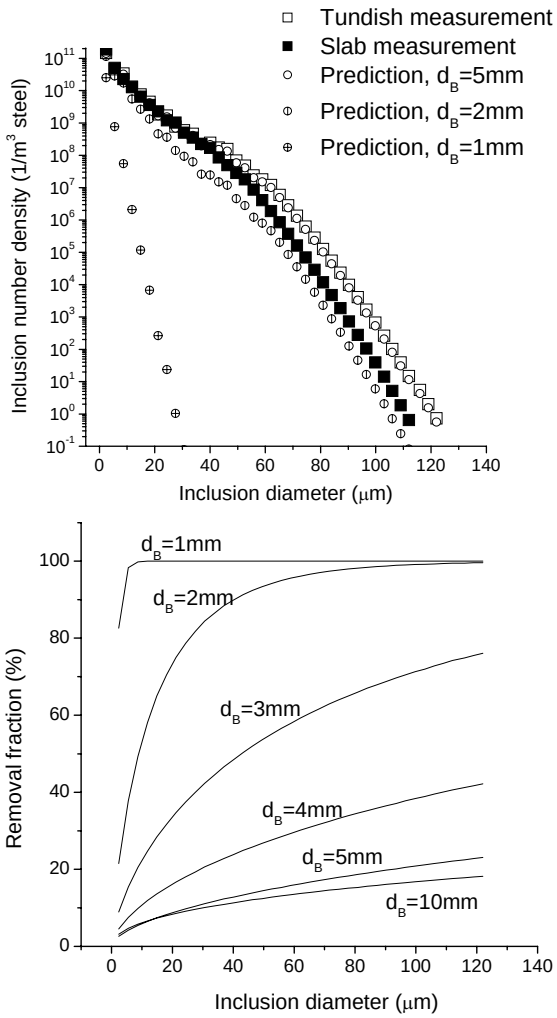

Fig. 11 Measured and calculated inclusion size distribution with different size bubble flotation (15 Nl/min gas)

As shown in Figure 12, increasing gas flow rate causes more inclusion removal by bubble flotation. Considering the effect of turbulent Stochastic motion slightly increases the inclusion removal by bubble flotation. For the current CC conditions, including a gas flow rate of 15 Nl/min, the bubble size is likely to be around 5mm, assuming there are a large number of active sites on the porous refractory that cause a gas flow rate of <0.5 ml/pore.[17] As shown in Figure 12, about 10% total oxygen is removed by bubble flotation. Previous work on this project indicate that ~8% of the small inclusions are removed to the top surface due to flow transport in the CC mold region.[47] Thus, the total predicted inclusion removal by flow transport and by bubble flotation is around 18%. The measured inclusion mass fraction is 66.8ppm in the tundish, and averages 51.9ppm in the slab, which corresponds to 22% removal in the mold (Fig.11). The prediction and the measurement agree remarkably well, considering that

some inclusions are likely entrapped to the SEN walls to cause clogging.

Decreasing bubble size is shown in Figs.11 and 12 to be more efficient at removing inclusions. As discussed before, however, small bubbles, such as those < 1mm, may be trapped into solidifying shell while moving through the lower recirculation zone. Thus, there should be an optimum bubble size, which gives not only high inclusion removal efficiencies, but also low entrapment rates. The present results suggest an optimal range of perhaps 2-4mm.

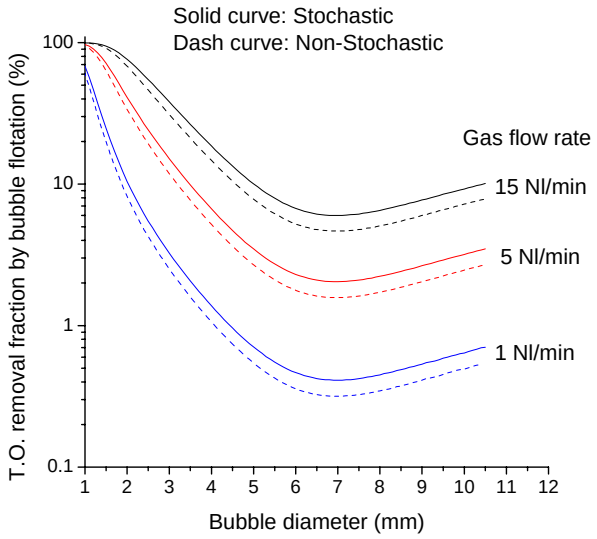

Fig. 12 Calculated inclusion removal by bubble flotation

8.4 Conclusions: This work presents a fundamental model of inclusion removal due to bubble flotation in molten steel processing. The model is validated with available measurements and applied to predict the changes in inclusion distribution that occur in the mold region of a continuous slab caster. Specific model findings include:

- Smaller bubbles and larger inclusions have larger attachment probabilities. Bubbles smaller than 1mm diameter have inclusion attachment probabilities as high as 30%, while the inclusion attachment probability for bubbles larger than 5mm is less than 1%. The stochastic effect of turbulence (modeled by the random walk method) slightly increases the attachment rate.
- In the CC strand, smaller bubbles penetrate and circulate more deeply than larger ones. Bubbles larger than 1mm mainly move in the upper roll. 0.2mm bubbles can move as far as 6.65m and take 71.5s before they either escape from the top or are entrapped through the bottom, while 0.5mm bubbles move 3.34m and take 21.6s, 1mm bubbles move 1.67m and take 9.2s, and 5mm bubbles move 0.59m and take 0.6s.
- In the CC mold, if bubbles are ~ 5mm in diameter, ~10% of the inclusions are predicted to be removed by bubble flotation, corresponding to around 3ppm decrease in total oxygen. Combined with ~ 8% inclusion removal by flow transport, the total roughly agrees with the measured inclusion removal rate by the CC mold of ~22%.
- Smaller bubbles are more efficient at inclusion removal by bubble flotation, so long as they are not entrapped in the solidifying shell. Larger gas flow rate favors inclusion removal by bubble flotation. The optimum bubble size should be 2-4mm.

9. Parametric Study: Flow Optimization Using Water Models: In this sub-section of the project, fluid flow parameters in a SEN and mold of a slab continuous caster are investigated using water models, numerical simulations and industrial measurements. In the water model, the top surface fluctuation, the pressure near the jet impingement point on the narrow face, and the flow patterns are measured. The effects of the submergence depth, SEN geometry, mold width, water flow rate, and gas flow rate are investigated. Three-dimensional fluid flow in the water model of the tundish, the SEN and the mold are calculated with numerical simulations, solving the continuity equation, momentum equations, turbulent energy and its dissipation rate equations using Fluent.[77] The trajectories of inclusions and bubbles are predicted by considering the buoyancy and drag forces acting on the bubbles and including the effect of turbulent fluctuations of the fluid flow with the Random-Walk model (Eq.[12]). In the industrial trial, the thickness of the liquid flux, inclusions in the steel, and inclusion removal to the mold flux are measured. The effect of the SEN well shape on the steel cleanliness is investigated.

9.1 Water Model Experiments and Similarity Criterion: The Weber-Froude similarity criterion is used to design the water model for the gas-water two phase fluid flow phenomena. Using the geometry scale factor λ=0.6, both Froude similarity and Weber similarity can be satisfied simultaneously. The relationship between the water flow rate Q_w and the molten steel throughput Q_S (m^3/hour) is then Q_w/Q_s=0.279.

A straight-mold steel caster of a 200mm thick and 1250mm wide strand is modeled with a clear plastic water model that is 1200mm in length, 120mm in thickness, and varies in width from 774.6mm at the top to 753.3mm at the bottom. A second strand width of 900mm is modeled with a top width of 557.7mm, and

bottom width of 542.4mm. The N_2 gas, used to model the argon gas in the molten steel, is injected into the mold through a central circular hole (4mm in diameter) in the bottom of the stopper rod. To stabilize casting speed, the water heights in the tundish and in the mold are first adjusted to be steady by adjusting the flow meter and the position of the stopper rod. The water height in the tundish is 600mm if not specified otherwise.

The definition of the level fluctuation is the mean of the 5 largest level fluctuations during each 40s measurement. This is because large level fluctuations account more for the slag entrainment than small ones. There should be some surface flow, including level fluctuations at the meniscus, in order to prevent the meniscus from freezing, but it should not be excessive to induce slag entrainment. Level fluctuations of 6-9mm at the meniscus of continuous-cast cold-rolled coil was reported to have the fewest surface defects.[78] This corresponds to optimal level fluctuations in the water model of 3.6-5.4mm. The level fluctuation at ¼ width should be as small as possible.

The impingement pressure is the mean of the measured pressure for 40s measured near the impingement point of the narrow face, subtracting the static water pressure ($\rho_w gh$). Lower pressures might be better. The lower roll location is the distance from the top surface to the center of the lower roll. Smaller values should improve inclusion removal to the top surface. Of these parameters, the most important is the magnitude of the level fluctuations.

The effects of casting speed (1.0-1.8m/min), SEN submergence depth (40-160mm), gas flow rate (0-18.32 Nl/min), SEN outport angle ($+5^o$- -25^o), inner diameter of SEN (30-50mm), the area ratio ψ (the area of the SEN bore to the total area of the two outports) (0.67-0.40), and the bottom well shape on the level fluctuation, the impingement pressure and the location of the lower roll center are investigated.

9.2 Multiphase Fluid Flow Pattern in the SEN: Three kinds of fluid flow pattern were observed in the SEN: bubbly flow, annular flow and critical flow between these two. For the bubbly flow pattern, the water and the gas are well mixed, and the jets at the two outports are relatively uniform and symmetrical. The turbulence in the SEN is very strong, so both the liquid phase and the gas phase have large energy losses, leading to a small jet energy and low impingement pressure at the narrow face. In addition, the strong interaction between the gas and the liquid in the SEN tends to dislodge any inclusions just attached to the SEN walls, which lowers the tendency for clogging.

For the annular flow pattern, the liquid annularly enters the SEN and then flows down along the walls, as it periodically changes its position. The liquid flow separates from the gas, which forms large pockets just below the stopper. The energy loss is small, so the impingement pressure to the narrow face is high. The flow is unstable, so the jets from the two outports tend to be asymmetrical. A given outport may emit more gas and less water, as the large gas regions escape and move intermittently along the outer walls of SEN to the top surface, where they rupture. This creates large level fluctuations and even generates foam near the SEN. At the other outport, there may be more water and less gas, which gives the jet more momentum and speed, leading to high impingement pressure on the narrow face, and big level fluctuations at the meniscus.

For the critical flow pattern, part of the inside of the SEN is bubbly flow, and the rest is annular flow. A tiny change of the water height in the tundish, casting speed, or gas flow rate can switch this critical flow to annular flow or to bubbly flow. If the flow regime suddenly switches to annular flow, the resistance to flow increases, which causes the water height in the tundish to increase abruptly, and the level in the mold to decrease abruptly. Water may even overflow the tundish. If the flow regime suddenly switches to bubbly flow, the resistance to flow decreases, which causes the water height in the tundish to decrease abruptly, and the level in the mold to increase abruptly. Water may even overflow the mold.

The flow pattern in the SEN with a fixed bore diameter is mainly affected by the liquid flow rate, the gas flow rate, and the liquid height in the tundish, as shown in Figure 13. When the casting speed is increased, the gas flow rate required to obtain bubbly flow is also increased. In order to achieve the bubbly flow pattern in the SEN, the operation conditions should lie below the curves in Fig13a. Fig.13a can be redrawn into Fig.13b to estimate flow regimes in the steel continuous casting process.

For the continuous casting of the 200mm×1250mm steel slab with 1.1m/min casting speed and 1000mm steel height in the tundish, the argon gas flow rate should be below 6.5 Nl/min to get the bubbly flow pattern in the SEN. However, in the real continuous casting process at Panzhihua steel, the gas flow rate is 10-20Nl/min, under which the flow in the SEN is the annular flow pattern, inducing the biased flow pattern in the mold, serious level fluctuation and slag entrainment. In the continuous caster, the periodic "jumping of the fish"— open eye of the molten steel induced by the serious level fluctuation at the ¼ width of the mold is observed. After using the optimized SEN configuration and with suitable gas flow rate, this phenomenon of

"jumping of the fish" is finally diminished. At some special cases such as the ladle change period, the steel height in the tundish and the casting speed decrease, the gas flow rate should be much smaller in order to achieve bubbly flow in the SEN.

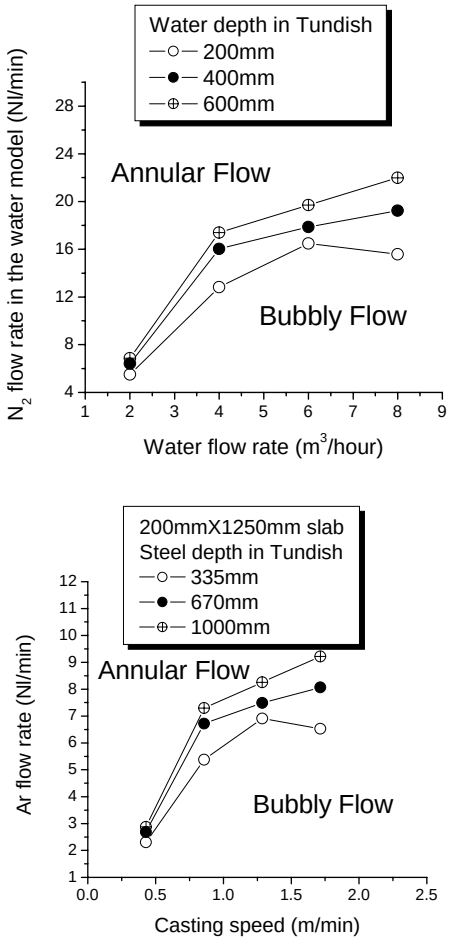

Fig.13 The conditions to achieve annular flow or the bubbly flow in a 45 mm SEN (water model (upper figure), and a 75 mm SEN (liquid steel, lower figure)

9.3 Multiphase Fluid Flow Pattern in the Mold: There are two main flow patterns in the mold: single roll and double roll. The single roll flow pattern is more likely with high gas injection, small SEN submergence depth and small casting speed. The double roll flow pattern is manly induced by large casting speed, large SEN submergence depth, and small gas flow rate. The fluid flow simulation shows that the single phase fluid flow pattern is usually double roll. There is little backflow at the outlet ports of the SEN. The jet impinges the narrow face, where part of the flow moves upwards along the narrow face to form the upper roll, and another part flows downwards to generate the lower roll.

At optimal levels, bubbles injected into the nozzle are helpful by reducing nozzle clogging, changing the fluid flow pattern, helping to capture and thereby remove inclusions, and decreasing the impingement pressure at the narrow face. Increasing gas injection encourages a single roll flow pattern, which tends to increase top surface fluctuations. Decreasing casting speed with the same gas injection also encourages the single roll flow pattern. Low gas flow tends to cause a double-roll flow pattern, while a high argon flow rate induces single-roll flow. To maintain a stable double-roll flow pattern, which is often optimal, the argon should be kept safely below a critical level. Excessive argon injection may generate transient variations of the jets entering the mold, introduce asymmetry in the mold cavity and increase surface turbulence. It is especially important to keep nearly constant liquid steel level in the mold, constant powder feeding rate, constant casting speed, constant gas injection fraction, constant slide gate opening, and fixed nozzle position (alignment and submergence).

9.4 Optimization of Fluid Flow in the SEN and the Mold: Level fluctuations are mainly induced by the jet impingement and upwards flow along the narrow face, rupture of bubbles at the top of the liquid, the single roll flow pattern in the mold, the transient biased fluid flow in the mold especially with gas injection, and the turbulence itself. Level fluctuations at the meniscus increase with increasing gas flow rate (Figure 14). When the casting speed is low, the gas mainly exits the top surface near the SEN. So level fluctuations are worse near the SEN. With high casting speed, the bubbles tend to exit closer to the narrow face, where level fluctuations become larger. Under the same conditions, the smaller width slab has a larger level fluctuation. This is because the turbulent energy is more easily dissipated in the larger slab. For the same conditions, the meniscus region generally has smaller level fluctuations than the interior. To obtain 3.6-5.4mm level fluctuations at the narrow face meniscus, the gas flow rate for the 1250mm width slab should be 5.3.-6.9 Nl/min, and for the 900mm width slab, the gas flow rate should be smaller than 4.6-7.6 Nl/min.

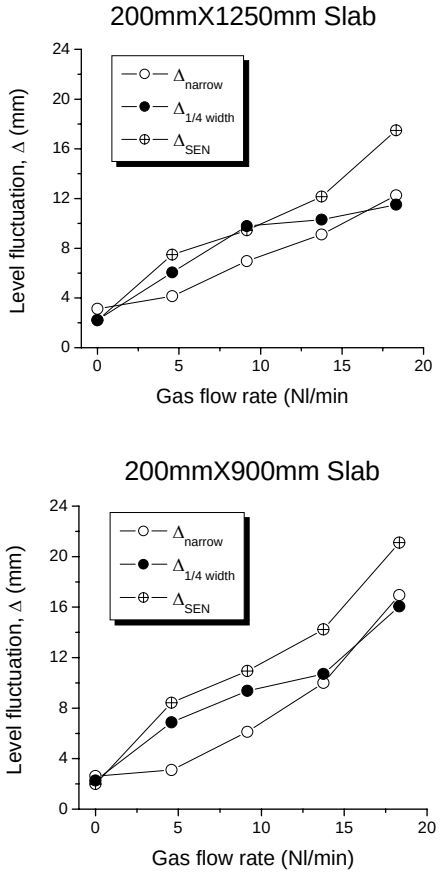

Fig. 14 Level fluctuations with different gas flow rates

Past work has found that larger casting speed tends to induce larger level fluctuations at the meniscus. For the configurations studied in this work, however, it is found that casting speed has little effect on the level fluctuations. This is likely due to compensating changes in the flow pattern. For example, increasing speed tends to switch from a single to a double roll flow pattern (decreasing surface velocities). This may offset the general increase in surface velocity caused by the higher speed. Moreover, flow stability and transient oscillation, which is most responsible for level fluctuations, is not directly related to speed when gas is present.

Level fluctuations at the meniscus decrease with increasing submergence depth to about 70 mm. Further increases in submergence depth deeper than 100m causes level fluctuations to increase again. The reason for this small effect is related to the tendency to switch from single to double-roll flow pattern with increasing submergence depth. The best submergence depth is around 70-100mm, with 5.1mm level fluctuation at meniscus for the 1250mm width, and 5.7mm for the 900mm width.

As shown in Figure 15, the level fluctuations decrease with increasing bore diameter of the SEN. This is perhaps due to decreasing the size of the channel between the SEN outer bore and the mold walls. This prevents communication between the two sides of the mold, which tends to discourage flow asymmetry and the associated level fluctuations. The optimal inner diameter of the SEN is 45mm for both the 900mm and 1250mm widths. With this bore size, the level fluctuations at the meniscus are 7.27mm for the 900mm width, and 5.32mm for the 1250mm width.

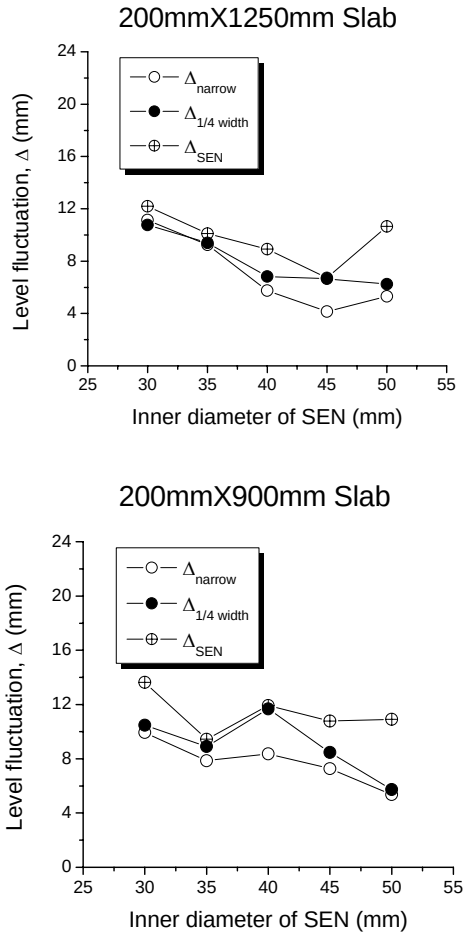

Fig.15 Effect of inner bore diameter of SEN on level fluctuations in the mold

Water model results also show that level fluctuations decrease slightly with increasing the port-to-bore area ratio ψ. This is due to lowering the exit velocity. However, if the area ratio is too big, it is possible to generate asymmetrical flow. For the 900mm width, the impingement pressure increases with increasing casting speed and decreasing inner diameter of the SEN. The impingement pressure is smallest for the 900mm width if the gas flow rate is 9.2Nl/min, the outport angle is downwards 15^{o}, and the submergence

depth is 100mm. If the area ratio is smaller than 0.57, the impingement pressure decreases with increasing area ratio. For the same conditions, the impingement pressure for the 1250mm width is smaller than for the 900mm width. For the 1250mm width, the impingement pressure is independent of the submergence depth and the bore diameter of the SEN. Figure 18 shows the effects of process parameters on the depth of the center of the lower recirculation roll. This point becomes deeper with increasing casting speed, decreasing gas flow rate, decreasing submergence depth, or decreasing SEN bore diameter.

Two kinds of well shape of the SEN are investigated: pointed bottom SEN and recess well SEN. Water model experiments with the 200mm×1250mm mold are performed with these two bottom shapes for the chosen optimal SEN configuration with 4.6 Nl/min gas flow rate and 90mm submergence depth. The water model results indicate that for the pointed bottom SEN, the level fluctuations at the meniscus is too small, which may not provide good heat transfer at the meniscus and all the meniscus region to freeze. Also, the pointed bottom SEN has larger level fluctuations near the SEN than the recess bottom SEN, likely owing to its being prone to flow asymmetry. It also has larger impingement pressure, and greater impingement depth, which is not good for inclusion removal in the mold.

The level fluctuations at the meniscus near the narrow face are smaller than those in the interior (centerline) at the ¼ width or near the SEN. They also indicate that level fluctuations for the 900mm width are larger than for the 1250mm width. A common SEN configuration is chosen for both slab widths: 45mm inner diameter, downwards 15°, 0.45 area ratio, and with recess well bottom shape.

9.5 Industrial Measurement of Steel Cleanliness with Different SEN Bottom Shapes: Industrial trials were performed for a 3-heat sequence (240 tonne total) cast with a slab size of 200mm×1250mm, and casting speed of 1.0-1.2m/min. To trace the origin of inclusions caused by mold slag entrainment, La_2O_3 is added to the mold flux before casting. The caster has two strands: strand 1 is with the recess well SEN, and strand 2 is with pointed-bottom SEN. The thickness of the liquid slag is measured at 10mm from the narrow face, at the ¼ width centerline, and 10mm from the SEN. Liquid flux samples are taken to analyze the change in Al_2O_3 content during continuous casting. Steel samples are taken from the mold at the ¼ width and 100 mm below the surface of the molten steel to analyze the total oxygen and the nitrogen in the steel. Slab samples are taken to observe micro inclusions with an optical microscope and large inclusions (>50μm) with Slime tests.[42] The microscope observations indicate that strand 2 (pointed-bottom SEN) has lower cleanliness.

The measured thickness of the liquid flux layer is shown in Table II. The liquid flux at the narrow-face meniscus is 1-3mm thicker than that at ¼ width and near the SEN. The recess-well SEN generates 3mm more liquid flux thickness than the pointed-bottom SEN. POSCO reported that for the low carbon Al-killed steel, if the casting speed is 1.0-1.6m/min, the best thickness of the liquid slag layer is 10-15mm.[79] In the current investigation, Strand 2 (pointed-bottom SEN) had insufficient slag layer thickness. This could disrupt meniscus solidification, leading to deep hooks, which can capture bubbles and inclusions. This might explain the lower cleanliness observed for the pointed-bottom SEN.

Inclusion absorption from the molten steel into the liquid flux on top of the mold has 2 components: 1) increasing the Al_2O_3 content from the mold powder composition (2.84% Al_2O_3) to the measured alumina concentration at steady state and 2) maintaining that value as flux is consumed. Based on the measured liquid flux thickness (Table II) and assuming a liquid slag density of 3500 kg/m^3, the mass of the liquid slag layer is 10.59kg (strand 1) and 8.46kg (strand 2). This corresponds to 0.47kg of Al_2O_3 from the steel (strand 1) and 0.44kg (strand 2), as given in Table VII. Next, based on the mold flux consumption rate of 0.5 kg/tonne, and total of 120 tonnes of steel cast per strand during the sequence, the total liquid slag consumed from the top surface is 60kg per strand . Multiplying by the percent Al_2O_3 increase in the liquid slag layer in Table III gives a consumed mass of 2.63 kg (strand 1), and 3.15 kg (strand 2). Dividing the total increase (3.10kg strand 1 and 3.59kg strand 2) over the entire heat (120 tonnes per strand) and converting from alumina (102g/mol) to oxygen (48g/mol) gives 12.2ppm total oxygen removed from the steel (strand 1) and 14.7ppm (strand 2).

The mean of the total oxygen of the molten steel in the mold with recess bottom SEN is around 59±35ppm. It is assumed that the total oxygen in the tundish entering both strands has similar total oxygen values. Then, inclusion removal is 20.7% from strand 1, and 23.9% from strand 2. This inclusion removal fraction by the mold slag matches the measured and simulated fractions of inclusions removed in the mold of a different 250mm×1300mm caster using a different measurement method.[47] Moreover, in the slab of strand 1, the total oxygen is estimated to be 59×(100%-20.7%)=47±28ppm, which matches well with the measurement of 47±20ppm total oxygen in a slab from this strand. The greater inclusion removal fraction from

strand 2 might be due to statistical variations, or it might indicate that mold slag entrainment is an important source of inclusions (not accounted for in this rough calculation) that is a more serious problem for the pointed bottom nozzle.

Table II Measured thickness of liquid slag layer on the top of the mold (mm)

	Near the meniscus	¼ width	Near the SEN	Mean thickness
Strand 1	14	13	12	12.9
	14	11	10	
	15	13	13	
Strand 2	11	10	10	10.3

Table III Measured Al_2O_3 fraction in the liquid flux of the mold and estimated total oxygen removal in the steel by SEN and the mold (initial Al_2O_3 content in the flux: 2.84%)

	Liquid slag on the top of the mold	Al_2O_3 fraction in the liquid slag (%)				ΔAl_2O_3 in liquid slag		Rough estimation of T.O. removal to the mold slag (ppm)
		Heat 1	Heat 2	Heat 3	Mean	%	kg	
Strand 1	10.59kg	9.08	6.89	5.71	7.23	4.39	0.465	12.2ppm
Strand 2	8.46kg	7.73	7.35	9.19	8.09	5.25	0.444	14.7ppm

Industry measurement shows that there is an abrupt increase in inclusions at the time of each ladle change. This may be induced by reoxidation from air absorption, slag entrainment in the tundish (due to emulsification during ladle opening or due to the lower tundish level), asymmetrical fluid flow from annular flow in the SEN induced by the low casting speed and other reasons. Furthermore, the starting and ending of casting have more inclusions than any other period. This is when the above air absorption and slag entrainment phenomena are the most extreme. The period of the ladle change (3.3-4.3mg inclusions 10kg steel) has twice the cleanliness problem of steady state pouring (1.6-2.2 mg inclusions per 10 kg steel). Many of the extracted inclusions by Slime method contain La_2O_3 tracer (Table VIII), indicating mold slag. This demonstrates that mold slag entrainment is a serious problem during continuous casting. Further efforts should focus on optimizing the mold flow pattern to decrease mold slag entrainment.

9.6 Conclusions:

- Three kinds of fluid flow pattern are observed in the SEN: bubbly flow, annular flow, and an intermediate critical flow structure. The annular flow structure induces detrimental asymmetrical flow in the mold. Moreover, its higher resistance to flow makes switching between flow structures prone to level fluctuations, which is even more detrimental.

- The SEN flow structure depends on the liquid flow rate, the gas flow rate, and the liquid height in the tundish. The gas flow rate should be adjusted with changes in the casting speed in order to maintain stable bubbly flow.

- Two main flow patterns are observed in the mold: single roll and double roll. The single roll flow pattern is generated by large gas injection, small SEN submergence depth and low casting speed. To maintain a stable double-roll flow pattern, which is often optimal, the argon should be kept safely below a critical level.

- The chosen optimal nozzle had 45mm inner bore diameter, downwards 15^{o}port angle, and 0.44 port-to-bore area ratio, and with recess bottom shape.

- Mass balances of inclusions in the steel slag from slag and slab measurements shows that around 22% inclusions are removed from the steel into the mold slag. However, entrainment of the mold slag itself is a critical problem. Inclusions in the steel increase two-fold during ladle changes. Slabs cast during the start and end of a sequence have the most inclusions.

10. Significant Findings: Advanced computational models are being developed to predict quantitatively, the removal of inclusions in the mold region during the continuous casting steel and related phenomena and processes. This multi-faceted research project includes the development and validation of models to predict transient fluid flow in the nozzle and mold, the transport of inclusion particles, the entrainment of particles from the top surface, the entrapment of inclusions by bubbles, the removal of particles to the top surface of the mold or their capture into the solidifying shell, and the optimization of fluid flow parameters to according to these findings. Work this past year has obtained several new findings, which are significant to the accurate prediction of inclusion behavior in continuous casting.

- Transient flow models require a fine mesh (400,00 nodes) to achieve accuracy within 17%.

- Although the safe removal of inclusion particles to the top surface increases with increasing particle size, the removal fractions are still small: only ~12% of 100 □m particles or 70% of 400□m particles are removed. Only 8% of small particles (10□m and 40□m) are removed.

- The removal of slag particles entrained from the top surface depends greatly on the particle size. Most (>92%) of the 250□m - 400□m droplets simply return to the slag layer. However, more than half of the 100□m particles are eventually captured, leading to sliver defects.

- Argon bubbles can remove significant quantities of inclusions, especially if they are small and are not captured into the final product. In the CC mold, if bubbles are ~ 5mm in diameter, ~10% of the inclusions are predicted to be removed by bubble flotation, corresponding to around 3ppm decrease in total oxygen. Combined with ~ 8% inclusion removal by flow transport, the total roughly agrees with the measured inclusion removal rate in the mold of ~22%.

- Mold flow parameters should be optimized to minimize level fluctuations and to avoid the entrainment of slag from the top surface. Specific gas flow rates and nozzle geometries to accomplish this are suggested for a particular set of casting conditions.

- Inclusions should be removed upstream of the mold, as much as possible, in order to minimize inclusion-based defects in the final product.

11. Impact: This work aims to improve understanding of the transient flow of molten steel and related phenomena during the continuous casting of steel slabs, through the development, validation, and application of fundamentally-based computational models. It further aims to predict quantitatively how inclusions are entrapped and to evaluate methods to lower inclusion-related defects. Plant observations have found that many serious quality problems, including inclusion entrapment, are directly associated with the flow pattern in the mold. The results from the computational simulations of this work have increased fundamental understanding of transient fluid flow, gas, and inclusion particle transport in the mold region. This has led to optimized nozzle geometry and gas flow rates to improve mold flow patterns and minimize inclusion defects from slag entrainment. Lowering defects from internal inclusions can improve steel minimum strength, fatigue life, surface appearance, yield and energy efficiency (from reduced rejects) and lower production cost. Furthermore, the computational tools developed and validated in this work can be applied to study and optimize flow in other processes.

12. Acknowledgments: The authors wish to thank the National Science Foundation (Grant # DMI-01-15486) and the Continuous Casting Consortium at the University of Illinois for support of this project. Thanks are also extended to industry researchers Ron O'Malley, formerly at AK Steel, P. Dauby, formerly at LTV Steel, S. Yang of Panzhihua Steel, X. Wang, K. Cai, J. Li, and X. Wan of University of Science and Technology, Beijing, and others who helped to obtain samples and plant data. The work of Jun Aoki on the bubble model subproject is acknowledged. Finally, thanks are due to FLUENT, Inc., for providing the FLUENT code, and to the National Center for Supercomputing Applications at the University of Illinois for computing time.

13. References:

1. "Continuously Cast Steel Output, 1999," Report, International Iron Steel Institute, Brussels, Belgium, 2000, www.worldsteel.org.
2. J. Herbertson, Q.L. He, P.J. Flint, R.B. Mahapatra, "Modelling of Metal Delivery to Continuous Casting Moulds," in Steelmaking Conf. Proc., Vol. 74, ISS, Warrendale, PA, (Washington, D.C.), 1991, 171-185.
3. T. Honeyands and J. Herbertson, "Oscillations in Thin Slab Caster Mold Flows," 127th ISIJ Meeting, ISIJ, Tokyo, Japan, 1994.
4. B.G. Thomas, "Application of Mathematical Models to the Continuous Slab Casting Mold.," Iron & Steelmaker (ISS Trans.), Vol. 16 (12), 1989, 53-66.
5. B.G. Thomas, "Mathematical Modeling of the Continuous Slab Casting Mold, a State of the Art Review," in Mold Operation for Quality and Productivity, A. Cramb, ed. Iron and Steel Society, Warrendale, PA, 1991, 69-82.
6. B.G. Thomas and F.M. Najjar, "Finite-Element Modeling of Turbulent Fluid Flow and Heat Transfer in Continuous Casting," Applied Mathematical Modeling, Vol. 15 (5), 1991, 226-243.
7. X. Huang, B.G. Thomas and F.M. Najjar, "Modeling Superheat Removal during Continuous Casting of Steel Slabs," Metall. Trans. B, Vol. 23B (6), 1992, 339-356.
8. X. Huang and B.G. Thomas, "Modeling of Steel Grade Transition in Continuous Slab Casting Processes," Metall. Trans., Vol. 24B (2), 1993, 379-393.
9. D.E. Hershey, B.G. Thomas and F.M. Najjar, "Turbulent Flow through Bifurcated Nozzles," Int. J. Num. Meth. in Fluids, Vol. 17 (1), 1993, 23-47.
10. B.G. Thomas and X. Huang, "Effect of Argon Gas on Fluid Flow in a Continuous Slab Casting Mold," in 76th Steelmaking Conf. Proc., Vol. 76, Iron and Steel Society, Warrendale, PA, (Dallas, TX), 1993, 273-289.

11. B.G. Thomas, X. Huang and R.C. Sussman, "Simulation of Argon Gas Flow Effects in a Continuous Slab Caster," Metall. Trans. B, Vol. 25B (4), 1994, 527-547.
12. G.D. Lawson, S.C. Sander, W.H. Emling, A. Moitra, B.G. Thomas, "Prevention of Shell Thinning Breakouts Associated with Widening Width Changes," in Steelmaking Conf. Proc., Vol. 77, ISS, Warrendale, PA, (Chicago, IL), 1994, 329-336.
13. F.M. Najjar, B.G. Thomas and D.E. Hershey, "Turbulent Flow Simulations in Bifurcated Nozzles: Effects of Design and Casting Operation," Metall. Trans. B, Vol. 26B (4), 1995, 749-765.
14. R. McDavid and B.G. Thomas, "Flow and Thermal Behavior of the Top-Surface Flux/ Powder Layers in Continuous Casting Molds," Metall. Trans. B, Vol. 27B (4), 1996, 672-685.
15. B.G. Thomas, A. Denissov and H. Bai, "Behavior of Argon Bubbles during Continuous Casting of Steel," in Steelmaking Conf. Proc., Vol. 80, ISS, Warrendale, PA., (Chicago, IL), 1997, 375-384.
16. B.G. Thomas, R. O'Malley, T. Shi, Y. Meng, D. Creech, D. Stone, "Validation of Fluid Flow and Solidification Simulation of a Continuous Thin Slab Caster," in Modeling of Casting, Welding, and Advanced Solidification Processes, Vol. IX, Shaker Verlag GmbH, Aachen, Germany, (Aachen, Germany, August 20-25, 2000), 2000, 769-776.
17. H. Bai and B.G. Thomas, "Bubble Formation during Horizontal Gas Injection into Downward Flowing Liquid," Metall. Mater. Trans. B, Vol. 32B (6), 2001, 1143-1159.
18. H. Bai and B.G. Thomas, "Turbulent Flow of Liquid Steel and Argon Bubbles in Slide-Gate Tundish Nozzles, Part I, Model Development and Validation," Metall. Mater. Trans. B, Vol. 32B (2), 2001, 253-267.
19. H. Bai and B.G. Thomas, "Turbulent Flow of Liquid Steel and Argon Bubbles in Slide-Gate Tundish Nozzles, Part II, Effect of Operation Conditions and Nozzle Design," Metall. Mater. Trans. B, Vol. 32B (2), 2001, 269-284.
20. H. Bai and B.G. Thomas, "Effects of Clogging, Argon Injection and Continuous Casting Conditions on Flow and Air Aspiration in Submerged Entry Nozzles," Metall. Mater. Trans. B, Vol. 32B (4), 2001, 707-722.
21. B.G. Thomas and H. Bai, "Tundish Nozzle Clogging – Application of Computational Models," in Steelmaking Conf. Proc., Vol. 18, Iron and Steel Society, Warrendale, PA, (Baltimore, MD), 2001, 895-912.
22. B.G. Thomas, "Modeling Study of Intermixing in Tundish and Strand during a Continuous-Casting Grade Transition," Iron and Steelmaker, Vol. 24 (12), 1997, 83-96.
23. X. Huang and B.G. Thomas, "Modeling of Transient Flow Phenomena in Continuous Casting of Steel," Canadian Metall. Quart., Vol. 37 (304), 1998, 197-212.
24. B.G. Thomas, H. Bai, S. Sivaramakrishnan, S.P. Vanka, "Detailed Simulation of Flow in Continuous Casting of Steel Using K-ε, LES, and PIV," International Symposium on Cutting Edge of Computer Simulation of Solidification and Processes, (Osaka, Japan, Nov. 14-16, 1999), ISIJ, 1999, 113-128.
25. B.G. Thomas and S.P. Vanka, "Study of Transient Flow Structures in the Continuous Casting of Steel," NSF Design & Manufacturing Grantees Conference, (Long Beach, CA), NSF, Washington, D.C., 1999.
26. B.G. Thomas and S.P. Vanka, "Study of Transient Flow Structures in the Continuous Casting of Steel," NSF Design & Manufacturing Grantees Conference, (Vancouver, Canada), NSF, Washington, D.C., 2000, 14p.
27. S.P. Vanka and B.G. Thomas, "Study of Transient Flow Structures in the Continuous Casting of Steel," NSF Design & Manufacturing Grantees Conference, (Jan. 7-10, Tampa, FL), NSF, Washington, D.C., 2001, 14p.
28. S. Sivaramakrishnan, H. Bai, B.G. Thomas, P. Vanka, P. Dauby, M. Assar, "Transient Flow Structures in Continuous Cast Steel," in Ironmaking Conference Proceedings, Vol. 59, ISS, Warrendale, PA, (Pittsburgh, PA, March 26-29, 2000), 2000, 541-557.
29. S. Sivaramakrishnan, B.G. Thomas and S.P. Vanka, "Large Eddy Simulation of Turbulent Flow in Continuous Casting of Steel," in Materials Processing in the Computer Age, Vol. 3, V. Voller and H. Henein, eds., TMS, Warrendale, PA, 2000, 189-198.
30. B.G. Thomas, "Modeling of the Continuous Casting of Steel: Past, Present, and Future, Dr. J. Keith Brimacombe Lecture," in Electric Furnace Conf. Proc., Vol. 59, ISS, Warrendale, PA, (Phoenix, AZ), 2001, 3-30.
31. W.H. Emling, T.A. Waugaman, S.L. Feldbauer, A.W. Cramb, "Subsurface Mold Slag Entrainment in Ultra-Low Carbon Steels," in Steelmaking Conf. Proc., Vol. 77, ISS, Warrendale, PA, (Chicago, IL), 1994, 371-379.
32. R.C. Sussman, M. Burns, X. Huang, B.G. Thomas, "Inclusion Particle Behavior in a Continuous Slab Casting Mold," in 10th Process Technology Conference Proc., Vol. 10, Iron and Steel Society, Warrendale, PA, (Toronto, Canada, April 5-8, 1992), 1992, 291-304.
33. B.G. Thomas, Q. Yuan, L. Zhang, S.P. Vanka, "Flow Dynamics and Inclusion Transport in Continuous Casting of Steel," in 2003 NSF Design, Service, and Manufacturing Grantees and Research Conf. Proceedings, R.G. Reddy, ed. University of Alabama, Tuscaloosa, AL 35498, (Burmingham, AL), 2003, 2328-2362.
34. B.G. Thomas, Q. Yuan, L. Zhang, B. Zhao, S.P. Vanka, "Flow Dynamics and Inclusion Transport in Continuous Casting of Steel," 2004 NSF Design, Service, and Manufacturing Grantees and Research Conf. Proceedings, (Dallas, TX), Southern Methodist University, Dallas, TX, 2004, T/BGT/1-41.
35. B.G. Thomas and T. Morthland, "3-D Heat Transfer Analysis of Columbus Slab Casting Mold," Report, Research Report to Columbus Steel, 2001.
36. B.G. Thomas, "Modeling of the Continuous Casting of Steel: Past, Present, and Future, Dr. J. Keith Brimacombe Lecture," Metal. & Material Trans., Vol. 33B (Dec.), 2002, 795-812.
37. B.G. Thomas, Q. Yuan, L. Zhang, S.P. Vanka, "Flow Dynamics and Inclusion Transport in Continuous Casting of Steel," in 2002 NSF Design, Service, Manufacturing and Industrial Innovation Research Conf. Proceedings, National Science Foundation, Washington, D.C., (San Juan, Puerto Rico), 2002, 22p.

38. L. Zhang, W. Pluschkell, and B.G. Thomas, "Nucleation and Growth of Alumina Inclusions During Steel Deoxidation," in Steelmaking Conf. Proc., Vol. 85, ISS, Warrendale, PA, (Nashville, March 10-13, 2002), 2002, 463-476.
39. L. Zhang, B.G. Thomas, X. Wang, and K. Cai, "Evaluation And Control Of Steel Cleanliness - A Review," in Steelmaking Conf. Proc., Vol. 85, ISS, Warrendale, PA, (Nashville, TN, March 10-13, 2002), 2002, 431-452.
40. L. Zhang and B.G. Thomas, "Alumina Inclusion Behavior During Steel Deoxidation," 7th European Electric Steelmaking Conference, (May 26-29, 2002, Venice, Italy), Associazione Italiana di Metallurgia, Milano, Italy, Vol. 2, 2002, 2.77-2.86.
41. B.G. Thomas, "Annual Report to Continuous Casting Consortium," Report, University of Illinois at Urbana-Champaign, 2002.
42. L. Zhang and B.G. Thomas, "State of the Art in Evaluation and Control of Steel Cleanliness," ISIJ International, Vol. 43 (3), 2003, 271-291.
43. Y. Meng and B.G. Thomas, "Heat Transfer and Solidification Model of Continuous Slab Casting: CON1D," Metal. & Material Trans., Vol. 34B (5), 2003, 685-705.
44. Y. Meng and B.G. Thomas, "Interfacial Friction-Related Phenomena in Continuous Casting with Mold Slags," in ISSTech 2003 Steelmaking Conf. Proc., Vol. 86, ISS, Warrendale, PA, (Indianapolis, IN, Apr. 27-30, 2003), 2003, 589-606.
45. Y. Meng and B.G. Thomas, "Interfacial Friction-Related Phenomena in Continuous Casting with Mold Slags," Metall. & Materials Trans. B, Vol. 34B (5), 2003, 707-725.
46. Q. Yuan, B.G. Thomas and S.P. Vanka, "Turbulent Flow and Particle Motion in Continuous Slab-Casting Molds," in ISSTech 2003 Process Technology Proceedings, Vol. 86, ISS, Warrendale, PA, (Indianapolis, IN, Apr 27-30, 2003), 2003, 913-927.
47. L. Zhang, B.G. Thomas, Kaike Cai, Jian Cui, L. Zhu, "Inclusion Investigation during Clean Steel Production at Baosteel," in ISSTech 2003 Steelmaking Conf. Proc., Vol. 86, ISS, Warrendale, PA, (Indianapolis, IN, Apr. 27-30, 2003), 2003, 141-156.
48. Q. Yuan, S.P. Vanka and B.G. Thomas, "Large Eddy Simulations of Transient Flow during Continuous Slab Casting of Steel," in 3rd International Symposium on Turbulenece and Shear Flow Phenomena, Vol. 2, (Sendai, Japan, June 25-27, 2003), 2003, 681-686.
49. L. Zhang and B.G. Thomas, "Inclusions in Continuous Casting of Steel", XXIV National Steelmaking Symposium,," in XXIV National Steelmaking Symposium, (Morelia, Mich, Mexico, Nov. 26-28, 2003), 2003, 138-183.
50. L. Zhang and B.G. Thomas, "Fluid Flow and Inclusion Motion in the Continuous Casting Strand," in XXIV National Steelmaking Symposium, (Morelia, Mich, Mexico, Nov. 26-28, 2003), 2003, 184-198.
51. L. Zhang and B.G. Thomas, "Inclusion Nucleation, Growth, and Mixing during Steel Deoxidation," Report No. CCC200206, University of Illinois at Urbana-Champaign, 2003.
52. Q. Yuan, B.G. Thomas and S.P. Vanka, "Study of Transient Flow and Particle Transport during Continuous Casting of Steel Slabs, Part 1. Fluid Flow," Metall. & Materials Trans. B, submitted August, 2003.
53. Q. Yuan, B.G. Thomas and S.P. Vanka, "Study of Transient Flow and Particle Transport during Continuous Casting of Steel Slabs, Part 2. Particle Transport," Metall. & Materials Trans. B, accepted October, 2003.
54. B.G. Thomas, "Continuous Casting," in Yearbook of Science and Technology, McGraw-Hill, (New York), 2004, 62-65.
55. Q. Yuan, B.G. Thomas and S.P. Vanka, "Study of Transient Flow and Particle Transport during Continuous Casting of Steel Slabs, Part 1. Fluid Flow," Metal. & Material Trans. B., Vol. 35B (4), 2004, 685-702.
56. Q. Yuan, B.G. Thomas and S.P. Vanka, "Study of Transient Flow and Particle Transport during Continuous Casting of Steel Slabs, Part 2. Particle Transport.," Metal. & Material Trans. B., Vol. 35B (4), 2004, 703-714.
57. B. Zhao, S.P. Vanka and B.G. Thomas, "Numerical Study of Flow and Heat Transfer in a Molten Flux Layer," Int. J. Heat and Fluid Flow, 2004, in press.
58. Q. Yuan, S. Sivaramakrishnan and B.G. Thomas, "Computational and Experimental Study of Turbulent Flow in a 0.4-Scale Water Model of a Continuous Steel Caster," Metal. & Material Trans. B., 2004,
59. B.G. Thomas, "Recent Advances in Computational Modeling of Continuous Casting Steel," Scanmet II Conference, (Lulea, Sweden), MEFOS, Vol. Vol. 1, 2004, 243-252.
60. B.G. Thomas, "Computational Modeling of Flow, Heat Transfer, and Deformation in the Continuous Casting of Steel," First Baosteel Annual Academic Conference, (Shanghai, China), Vol. Vol. 1, 2004, 13-19.
61. L. Zhang, S. Yang, X. Wang, K. Cai, J. Li, X. Wan, B.G. Thomas, "Physical, Numerical and Industrial Investigation of Fluid Flow and Steel Cleanlines in the Continuous Casting Mold at Panzhihua Steel," AISTech 2004, (Nashville, TN), Assoc. Iron Steel Technology, 2004.
62. L. Zhang, J. Aoki and B.G. Thomas, "Inclusion Removal by Bubble Flotation in Continuous Casting Mold," Materials Science & Technology 2004, (New Orleans, LA), TMS, Warrendale, PA, 2004.
63. Q. Yuan, B. Zhao, S.P. Vanka, B.G. Thomas, "Study of Computational Issues in Simulation of Transient Flow in Continuous Casting," Materials Science & Technology 2004, (New Orleans, LA), TMS, Warrendale, PA, 2004.
64. Q. Yuan, B. Zhao, S.P. Vanka, B.G. Thomas, "Study of Computational Issues in Simulation of Transient Flow in Continuous Casting," Steel Research International, 2004, in press.
65. G. Wilde and J.H. Perepezko, "Experimental Study of Particle Incorporation During Dendritic Solidification," Materials Science & Engineering A, Vol. 283, 2000, 25-37.
66. J-H.Jeong, N. Goldenfeld and J.A. Dantzig, "Phase Field Model for Three-Dimensional Dendritic Growth with Fluid Flow," Physical Review E, Vol. 64, 2001, 1-14.
67. Q. Yuan, "Transient Study of Turbulent Flow and Particle Transport During Continuous Casting of Steel

Slabs," PhD Thesis, University of Illinois at Urbana-Champaign, IL, 2004.
68. W. Kurz and D.F. Fisher, Fundamentals of Solidification, Trans Tech Publications SA, Aedermannsdorf, Switzerland, 1984, 242.
69. Q. Yuan, "Modeling of Particle Engulfment / Pushing at Solidification Front during Continuous Casting of Steel," Report, University of Illinois at Urbana-Champaign, 2002.
70. W.H. Press, B.P. Flannery, S.A. Teukolsky, W.T. Vetterling, Numerical Recipes, Cambridge University Press, New York, NY, 1988, 963.
71. H. Shibata, H. Yin, S. Yoshinaga, T. Emi, M. Suzuki, "In-Situ Observation of Engulfment and Pushing of Nonmetallic Inclusions in Steel Melt by Advancing Melt/Solid Interface," ISIJ International, Vol. 38 (2), 1998, 149-156.
72. D.M. Stefanescu, F.R. Juretzko, B.K. Dhindaw, A. Catalina, S. Sen, "Particle Engulfment and Pushing by Solidifying Interfaces: Part Ii. Microgravity Experiments and Theoretical Analysis," Metallurgical and Materials Transactions A,, Vol. 29A, 1998, 1697-1706.
73. Q. Han and J.D. Hunt, "Particle Pushing: Critical Flow Rate Required to Put Particles into Motion," J. Crystal Growth, Vol. 152, 1995, 221-227.
74. Q. Han, "The Mechanisms for Particle Pushing," PhD Thesis, University of Oxford, Oxford, UK, 1994.
75. B.G. Thomas, R.J. O'Malley and D.T. Stone, "Measurement of temperature, solidification, and microstructure in a continuous cast thin slab," Modeling of Casting, Welding, and Advanced Solidification Processes, (San Diego, CA), TMS, Warrendale, PA, Vol. VIII, 1998, 1185-1199.
76. D. Gupta and A.K. Lahiri, "A Water Model Study of the Flow Asymmetry Inside a Continuous Slab Casting Mold," Metall. Mater. Trans. B, Vol. 27B (5), 1996, 757-764.
77. FLUENT6.1, Report, Fluent Inc., Lebanon, New Hampshire, www.fluent.com, 2003.
78. T. Teshima, J. Kubota, M. Suzuki, K. Ozawa, T. Masaoka, S. Miyahara, "Influence of Casting Conditions on Molten Steel Flow in Continuous Casting Mold at High Speed Casting of Slabs," Tetsu-to-Hagane, Vol. 79 (5), 1993, 576-582.
79. I.R. Lee, J. Chai and K. Shin, "Optimization Technology of Mold Powder According to Casting Conditions," in 71th Steelmaking Conference Proceedings, Vol. 71, ISS, Warrendale, PA, 1988, 175-180.